

# Supporting information for: Dynamical decoupling of nitroxides in *o*-terphenyl: a study of temperature, deuteration and concentration effects

Janne Soetbeer,<sup>a</sup> Miriam Hülsmann,<sup>b</sup> Adelheid Godt,<sup>b</sup> Yevhen Polyhach<sup>a</sup> and Gunnar Jeschke<sup>\*a</sup>

November 29, 2017

## 1 Syntheses of nitroxides 1 and 2

The synthetic routes for nitroxides **1** and **2** are briefly described in the main text. Sections 1.1 and 1.2 of the ESI provide a detailed discussion and section 1.3 the experimental procedures. Note that the synthesis scheme is given in the main text as Fig. 4. It provides the compound numbers used in the following.

### 1.1 Comment on the synthesis of nitroxide 1

The preparation of nitroxide **1** included the monomethylation of diol **3**. In case of a statistical reaction of diol **3** with one equivalent of the methylating agent methyl iodide, 50% of the monomethylation product, monool **4**, and 25% of starting diol **3** as well as of the dimethylation product are expected. That only 30% of monool **4**, 12% of the dimethylation product and 59% of starting material, diol **3**, were isolated, is ascribed to loss of methyl iodide during the reaction. Methyl iodide is a very volatile compound and for the concrete experiment only 27 mg were needed.

### 1.2 Comment on the synthesis of nitroxide 2

Nitroxide **2** was a synthetic intermediate in our work towards diradicals showing two nitroxides connected through a rodlike spacer of defined length and differing only in the isotopes of their hydrogen atoms and/or nitrogen atoms. This is the reason for the structural differences between nitroxides **1** and **2**: terminal hydroxy versus methoxy group and different lengths of rodlike units. There is an increasing interest in model compounds with pairs of two different spin labels (mixed diradicals), with nitroxide being one or none of the two spin labels. The syntheses of the concrete nitroxide **2** and its synthetic precursor **8b** provide information about the access to building blocks as well as guidelines for the preparation of mixed diradicals with other spacer lengths and/or other spin labels.

A fast access to nitroxide **2** would have been the reaction of readily available diol **8a**<sup>?</sup> with one equivalent of spin label **5b**. However, column chromatographical isolation of nitroxide **2** from a mixture with the corresponding dinitroxide and residual diol **8a**, as obtained in this statistical approach, turned out to be rather difficult. Considering in addition the analytical challenges when working with paramagnetic compounds, we assessed this route to be too risky for the synthesis of mixed diradicals having two nitroxides differing only in their isotopes.

When staying with diol **8a** as the starting material, one of the OH groups of diol **8a** had to be masked. Silylation of diol **8a** using one equivalent of *tert*-butyldimethylsilyl chloride (TBDMS-Cl) gave a mixture of diol **8a**, monosilylated diol **8c** (Fig. S1) and disilylated diol. These compounds were easily separated, however, the TBDMS group proved unreliable during the spin labeling of monosilylated diol **8c** with nitroxide **5a** using DCC and DMAP in CH<sub>2</sub>Cl<sub>2</sub>.

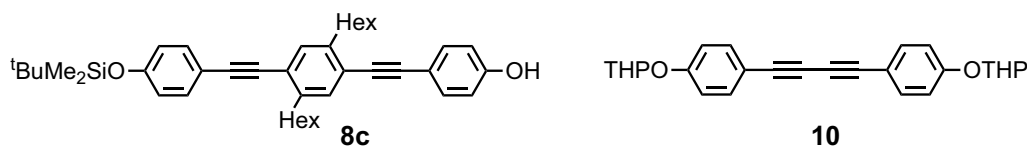


**Fig. S1.** Structural formulae of monosilylated diol **8c** and alkyne dimer **10**.

We turned to THP as the protecting group, because we had the necessary starting materials already in hand.<sup>??</sup> Thus, THP-protected diol **8b** was the new target compound. Instead of mono-functionalisation of diol **8a**, the different terminal groups of the spacer were implemented simultaneously with the spacer assembly. As illustrated in Fig. 4(b) of the main text, THP-protected diol **8b** was assembled via two routes. In one approach the THP group of THPO-alkyne **7b** was removed and the product, HO-alkyne **7a**, was coupled with THPO/iodo-tolane **6b** giving mono-protected diol **8b**. This approach resulted in a yield of only 38% with respect to THPO/iodotolane **6b**. More than 47% of THPO/iodo-tolane **6b** were recovered. This result was probably caused by the instability of HO-alkyne **7a**, which is a well soluble, slightly brownish oily material which turns into a violet insoluble material when kept for overnight at room temperature, even at reduced pressure (ca. 0.01 mbar).<sup>? ? §</sup> Therefore, HO-alkyne **7a** was used immediately after removing most of the solvent. The other approach towards THP-protected diol **8b** started with the deprotection of THPO/iodo-tolane **6b** to obtain HO/iodotolane **6a**, which, in contrast to HO-alkyne **7a**, showed no indication of degradation during the time we handled the material. Nevertheless, care has to be taken of the reaction time when deprotecting THPO-alkyne **7b** as the amount of unidentified side products increases with time. It is easier to chromatographically remove residual THPO-alkyne **7b** than the side products. Coupling of HO/iodo-tolane **6a** with THPO-alkyne **7b** gave a yield of 64% of monoprotected diol **8b** in respect to HO/iodo-tolane **6a**. Monoprotected diol **8b** was accompanied by the oxidative dimerization product of THPO-alkyne **7a**, the alkyne dimer **10**. This was either formed during the coupling reaction or the latest upon work-up when oxygen is no longer excluded. Despite the sufficiently different  $R_f$  values [ $R_f$  (monoprotected diol **8b**) = 0.3; alkyne dimer **10** ( $R_f$  = 0.5)], alkyne dimer **10** was difficult to separate and a trace of it remained, undetected by <sup>1</sup>H NMR spectroscopy and thin layer chromatography, in the sample of monoprotected diol **8b** that was used for the next synthetic step (see below). The difficulties experienced in chromatographic separation are attributed to tailing of alkyne dimer **10** caused by its very low solubility in CH<sub>2</sub>Cl<sub>2</sub>, which was the solvent used for chromatography.

Protection with a THP group proved to be compatible with the following step, the ester formation with spin label **5b** to obtain nitroxide **9**. Surprisingly, chromatography of the crude product gave not only nitroxide **9** but also a small amount of alkyne dimer **10**. This must be a relict of the previous synthetic step. Furthermore, after removal of the THP group of nitroxide **9** a trace of diol **8a** was isolated by chromatography manifesting that ester formation had not been complete and that the sample of nitroxide **9** contained monoprotected diol **8b**, which had gone undetected by thin layer chromatography, even though this analytical technique is highly sensitive to detect such compounds with light of 366 nm.

### 1.3 Experimental section

**General.** All reactions were performed in argon and in dried vessels. The argon was passed through a tube filled with anhydrous CaCl<sub>2</sub> prior use. Solutions were degassed through several freeze-pump-thaw cycles. Solvents used for reactions were of p.a. grade except of tetrahydrofuran (THF) which was distilled from Na/benzophenone, and dimethylformamid (DMF) which was purchased over molecular sieves. For work-up, extractions, and chromatography, solvents of technical grade were used after they had been distilled at 40 °C *in vacuo*. Solvents were removed at 40 °C

<sup>§</sup>Cevasco *et al.*<sup>?</sup> described 4-hydroxyphenylethyne (HO-alkyne **7a**) as a very unstable compound whereas Ting *et al.*<sup>?</sup> reported the synthesis of HO-alkyne **7a** with a yield of 99% without mentioning issues with stability.

and reduced pressure. Residual solvents were removed at room temperature and approx. 0.01 mbar.

Column chromatography was carried out on silica gel (40-63  $\mu\text{m}$ ) applying slight pressure. Below, the size of the column is given as diameter x length. Centrifugal chromatography using a chromatotron was performed on plates that had been prepared from Merck silica gel 60 PF<sub>254</sub>. The compounds were loaded onto the silica gel column or the chromatotron plate as concentrated solutions in the solvents used for chromatography, if not mentioned otherwise. Thin layer chromatography was carried out on silica gel coated aluminum foils (Merck, 60 F<sub>254</sub>). The spots were detected with UV light of  $\lambda = 254$  and 366 nm. The compositions of solvent mixtures are given in volume ratios.

NMR spectra were recorded at room temperature. The solvent was used for calibration:  $\text{CDCl}_3$ :  $\delta$  ( $^1\text{H}$ ) = 7.25,  $\delta$  ( $^{13}\text{C}\{^1\text{H}\}$ ) = 77.0;  $\text{CD}_2\text{Cl}_2$ :  $\delta$  ( $^1\text{H}$ ) = 5.32,  $\delta$  ( $^{13}\text{C}\{^1\text{H}\}$ ) = 53.8.  $^{13}\text{C}$  NMR signal assignment is supported by DEPT-135 experiments.

The melting points were determined in open capillaries.

$\text{PdCl}_2(\text{PPh}_3)_2$  was synthesized according to the literature,<sup>9</sup> however using 2.1 times the given amount of MeOH. Diol **8a**,<sup>9</sup> THPO-alkyne **7b**,<sup>9</sup> and THPO/iodo-tolane **6b**<sup>9</sup> were prepared as described. 1-Oxyl-2,2,5,5-tetramethylpyrroline-3-carboxylic acid (spinlabel **5a**) was commercially obtained. Perdeuterated 1-oxyl-2,2,5,5-tetramethylpyrroline-3-carboxylic acid (spinlabel **5b**) was provided by Herbert Zimmermann.

**Monool 4.** Diol **3** (148 mg, 0.19 mmol) was dissolved in THF (10 mL) and DMF (10 mL).  $\text{K}_2\text{CO}_3$  (54 mg, 0.39 mmol) and then MeI (0.6 mL of a solution prepared from 100  $\mu\text{L}$  of MeI and 5 mL of DMF, 0.19 mmol) were added. The suspension was stirred at 44 °C for 18 h. It was cooled with an ice bath and aqueous 5 N HCl (ca. 8 mL) was added. The aqueous phase was extracted with  $\text{CH}_2\text{Cl}_2$ , the combined organic phases were washed with aqueous 2 N HCl and then with water. They were dried with  $\text{Na}_2\text{SO}_4$  and finally the solvents were removed. Centrifugal chromatography of the residue (plate thickness: 2 mm; pentane/ $\text{CH}_2\text{Cl}_2$  1:2) gave subsequently dimethylation product (18 mg, 12%), monool **4** (45 mg, 30%), and diol **3** (88 mg, 59%), all as yellow solids. Monool **4** was freeze-dried using benzene.

Analytical data of monool **4**:  $^1\text{H}$  NMR (250 MHz,  $\text{CDCl}_3$ ):  $\delta = 7.45$  (half of AA'XX', 2 H, H meta to  $\text{OCH}_3$ ), 7.41 (half of AA'XX', 2 H, H meta to OH), 7.35 (s, 2 H, H ortho to Hex), 7.32 and 7.31 (2 hardly resolved s, together 2 H, H ortho to Hex), 6.89 (half of AA'XX', 2 H, H ortho to  $\text{OCH}_3$ ), 6.82 (half of AA'XX', 2 H, H ortho to OH), 4.81 (s, 1 H, OH), 3.83 (s, 3 H,  $\text{OCH}_3$ ), 2.76 (m, 4 H,  $\text{ArCH}_2$ ), 1.35 (m, 4 H,  $\text{ArCH}_2\text{CH}_2$ ), 1.35 (m, 24 H,  $\text{CH}_2$ ) 0.88 (m with two dominant lines at 0.89 and 0.87 ppm, 12 H,  $\text{CH}_2\text{CH}_3$ ). MS (Maldi-TOF with  $\alpha$ -cyano-4-hydroxycinnamic acid as the matrix; positive mode):  $m/z = 784.70$  ( $\text{M}^+$ ).

**Nitroxide 1.** To a solution of monool **4** (45 mg, 0.057 mmol), 1-oxyl-2,2,5,5-tetramethylpyrroline-3-carboxylic acid (spin label **5a**; 21.2 mg, 0.115 mmol) and 4-(dimethylamino)pyridine (14.1 mg, 0.115 mmol) in THF (4 mL) was added *N,N'*-dicyclohexylcarbodiimide (23.6 mg, 0.114 mmol). The reaction mixture was stirred at room temperature. After 1 h a precipitate had formed. After a reaction time of 4 d, the precipitate was filtered off and washed with THF (2 mL). The solvent of the filtrate was removed. In order to get rid of trapped THF, the crude product was suspended in  $\text{CH}_2\text{Cl}_2$  (2 mL) and the solvent was removed. Centrifugal chromatography of the residue (plate thickness: 1 mm;  $\text{CH}_2\text{Cl}_2$ ) gave a fraction containing nitroxide **1** and unidentified components. Centrifugal chromatography of this fraction (plate thickness: 1 mm; pentane/ $\text{CH}_2\text{Cl}_2$  1:1) gave nitroxide **1** (33 mg, 60%) as a yellow, slowly crystallising oil. It was freeze-dried using benzene.  $^1\text{H}$  NMR (250 MHz,  $\text{CD}_2\text{Cl}_2$ ): All signals are broadened and structureless.  $\delta = 7.52$  (br s, 2 H, H meta to ester group), 7.39 (apparent d,  $J = 8.5$  Hz, 2 H, H meta to  $\text{OCH}_3$ ), 7.31, 7.30 and 7.29 (3 strongly overlapping s, altogether 3 H, H ortho to Hex), 7.27 (s, 1 H, H ortho to Hex), 7.14 (very broad s, integration not reliably possible because of broadness and overlap with other signals, H ortho to ester group), 6.83 (apparent d,  $J = 8.5$  Hz, 2 H, H ortho to  $\text{OCH}_3$ ), 3.75 (s, 3 H,  $\text{OCH}_3$ ),

2.71 (m, 8 H, ArCH<sub>2</sub>), 1.60 (m, 8 H, ArCH<sub>2</sub>CH<sub>2</sub>), 1.29 (m, 24 H, CH<sub>2</sub>), 0.82 (m with two dominant lines at 0.83 and 0.81 ppm, 12 H, CH<sub>3</sub>). Elemental analysis calcd (%) for C<sub>66</sub>H<sub>80</sub>O<sub>4</sub>N (951.369): C 83.32, H 8.48, N 1.47; found C 83.32, H 8.47, N 1.51.

**HO/iodo-tolane 6a.** To a solution of THPO/iodo-tolane **6b** (2.00 g, 3.49 mmol) in THF (80 mL) and MeOH (60 mL) was added *p*-toluenesulfonic acid monohydrate (679 mg, 3.57 mmol). The reaction was monitored with thin layer chromatography (CH<sub>2</sub>Cl<sub>2</sub>). After 4.7 h at room temperature, Et<sub>2</sub>O and an aqueous solution of NaCl were added. The aqueous phase was extracted with Et<sub>2</sub>O, the combined organic phases were washed with an aqueous solution of K<sub>2</sub>CO<sub>3</sub>, then with aqueous 2 N HCl and finally with brine. After drying with MgSO<sub>4</sub>, the solvents were removed giving a pinkish orange solid. <sup>1</sup>H NMR spectroscopy revealed that about 2% of THPO/iodo-tolane **6b** had been left over. Therefore, the solid was dissolved in THF (40 mL) and MeOH (10 mL) and *p*-toluenesulfonic acid monohydrate (523 mg, 2.75 mmol) was added. After the solution had been stirred at room temperature for 5.5 h, work-up as described above was performed. This gave an orange-brown oil. Column chromatography of this oil (3.5 cm × 30 cm; CH<sub>2</sub>Cl<sub>2</sub>) gave first a brownish oil (28 mg) consisting mainly of THPO/iodo-tolane **6b**, then an orange colored solid (4 mg) of unknown identity, and finally HO/iodo-tolane **6a** (1.26 g, 74%) as a slightly orange solid. M.p.: 56-57 °C. <sup>1</sup>H NMR (250 MHz, CD<sub>2</sub>Cl<sub>2</sub>): δ = 7.69 (s, 1 H, H ortho to I), 7.42 (half of AA'XX', 2 H, H meta to OH), 7.30 (s, 1 H, H meta to I), 6.84 (half of AA'XX', 2 H, H ortho to OH), 5.23 (s, 1 H, OH), 2.74 and 2.66 (2 m, 2 H each, ArCH<sub>2</sub>), 1.62 (m, 4 H, CH<sub>2</sub>), 1.35 (m, 12 H, CH<sub>2</sub>), 0.91 and 0.88 (2 m, 3 H each, CH<sub>3</sub>). <sup>13</sup>C NMR (63 MHz, CD<sub>2</sub>Cl<sub>2</sub>): δ = 156.4 (C<sub>Ar</sub>O), 144.4 and 143.2 (C<sub>Ar</sub>Hex), 139.9 (CH ortho to I), 133.4 (CH meta to OH), 132.4 (CH meta to I), 123.4 (C<sub>Ar</sub>C≡C ortho to Hex), 116.02 (C<sub>Ar</sub>C≡C para to OH), 115.95 (CH ortho to OH), 100.7 (C-I), 93.7 and 86.7 (C≡C), 40.5, 34.2, 32.10, 32.07, 31.0, 30.6, 29.6, 29.4, and 23.0 (CH<sub>2</sub>), 14.2 (CH<sub>3</sub>). Elemental analysis calcd (%) for C<sub>26</sub>H<sub>33</sub>OI (488.454): C 63.93, H 6.81; found C 63.92, H 6.85.

**Monoprotected diol 8b.** To a degassed solution of HO/iodo-tolane **6a** (1.19 g, 2.44 mmol) and THPO-alkyne **7b** (518 mg, 2.56 mmol) in Et<sub>2</sub>NH (40 mL) were added Pd(PPh<sub>3</sub>)<sub>2</sub>Cl<sub>2</sub> (17 mg, 0.02 mmol) and CuI (9 mg, 0.05 mmol). After stirring the reaction mixture for 18 h at room temperature, Et<sub>2</sub>NH was distilled off at about room temperature and reduced pressure. The residue was dissolved in CH<sub>2</sub>Cl<sub>2</sub> and water. The aqueous phase was extracted with CH<sub>2</sub>Cl<sub>2</sub>, the combined organic phases were washed with a saturated aqueous solution of NH<sub>4</sub>Cl and dried with Na<sub>2</sub>SO<sub>4</sub>. The solvent was removed. Column chromatography of the residue (3.5 cm × 27 cm; CH<sub>2</sub>Cl<sub>2</sub>) gave four fractions: (1) brown oil (4 mg) of unknown identity; (2) slightly orange solid (89 mg) consisting of HO/iodo-tolane **6a**, alkyne dimer **10**, and monoprotected diol **8b** in a ratio of ca. 9:4:6; (3) slightly orange solid (504 mg) consisting of monoprotected diol **8b** and small amounts of HO/iodo-tolane **6a** and alkyne dimer **10**; (4) monoprotected diol **8b** (R<sub>f</sub> = 0.31; 541 mg, 39%) as a slightly orange solid. Column chromatography of the third fraction (3.0 cm × 35 cm; CH<sub>2</sub>Cl<sub>2</sub>) gave additional monoprotected diol **8b** (344 mg, 25%) as a slightly orange solid. For the second chromatography, the material had been adsorbed onto silica gel by dissolving the material in CH<sub>2</sub>Cl<sub>2</sub>, adding a small amount of silica gel, and removing the solvent (40 °C, reduced pressure). The resulting freely flowing powder was loaded onto the top of the silica gel column. M.p.: 89-90 °C. <sup>1</sup>H NMR (250 MHz, CD<sub>2</sub>Cl<sub>2</sub>): δ = 7.47 (half of AA'XX', 2 H, H meta to OTHP), 7.43 (half of AA'XX', 2 H, H meta to OH), 7.36 and 7.35 (2 s, 1 H each, H ortho to Hex), 7.06 (half of AA'XX', 2 H, H ortho to OTHP), 6.83 (half of AA'XX', 2 H, H ortho to OH), 5.46 (t, J = 3.2 Hz, 1 H, O<sub>2</sub>CH), 5.42 (s, 1 H, OH), 3.91 and 3.62 (2 m, 1 H each, OCH<sub>2</sub>), 2.81 (m, 4 H, ArCH<sub>2</sub>), 2.1-1.2 (m, 22 H, CH<sub>2</sub>), 0.90 (m, 6 H, CH<sub>3</sub>). <sup>13</sup>C NMR (63 MHz, CD<sub>2</sub>Cl<sub>2</sub>): δ = 157.7 (C<sub>Ar</sub>OTHP), 156.4 (C<sub>Ar</sub>OH), 142.53 and 142.49 (C<sub>Ar</sub>Hex), 133.5 (CH meta to OH), 133.1 (CH meta to OTHP), 132.5 (CH ortho to Hex), 123.0 (C<sub>Ar</sub>C≡C ortho to Hex), 117.0 (CH ortho to OTHP), 116.9 (C<sub>Ar</sub>C≡C para to OTHP), 116.1 (C<sub>Ar</sub>C≡C para to OH), 116.0 (CH ortho to OH), 96.9 (O<sub>2</sub>CH), 94.2, 94.1, 87.6, and 87.4 (C≡C), 62.6 (OCH<sub>2</sub>), 34.5, 32.2, 31.1, 30.7, 29.7, 25.6, 23.1 and 19.2 (CH<sub>2</sub>), 14.3 (CH<sub>3</sub>).

Elemental analysis calcd (%) for C<sub>39</sub>H<sub>46</sub>O<sub>3</sub> (562.794): C 83.23, H 8.24; found C 83.03, H 8.24.

**Monoprotected diol 8b via HO-alkyne 7a.** A solution of THPO-alkyne **7b** (266 mg, 1.32 mmol), *p*-toluenesulfonic acid monohydrate (260 mg, 1.37 mmol) in THF (30 mL) and MeOH (20 mL) was stirred for 3 h at room temperature. The work-up procedure described for the preparation of HO/iodo-tolane **6a** was followed. The obtained pale brownish oil (269 mg) containing the HO-alkyne **7a** and a substantial amount of MeOH and THF was used for the next reaction.

To a degassed solution of this oil and THPO/iodo-tolane **6b** (570 mg, 1.00 mmol) in Et<sub>2</sub>NH (10 mL) were added Pd(PPh<sub>3</sub>)<sub>2</sub>Cl<sub>2</sub> (7 mg, 0.01 mmol) and CuI (4 mg, 0.02 mmol). After stirring the reaction mixture for 19 h at room temperature, Et<sub>2</sub>NH was removed at about room temperature and reduced pressure. The residue was dissolved in Et<sub>2</sub>O and water. The aqueous phase was extracted with Et<sub>2</sub>O, the combined organic phases were washed with a saturated aqueous solution of NH<sub>4</sub>Cl and dried with Na<sub>2</sub>SO<sub>4</sub>. The solvent was removed. Column chromatography of the residue (3.0 cm × 32 cm; CH<sub>2</sub>Cl<sub>2</sub>) gave two fractions with substantial amounts of materials: first THPO/iodo-tolane **6b** (269 mg, 47%) as a beige solid, and, second, monoprotected diol **8b** (213 mg, 29% referring to THPO-alkyne **7b** over two steps, 38% referring to THPO/iodo-tolane **6b**). Fractions that were eluted between these two main fractions contained besides other components monoprotected diol **8b**.

**Nitroxide 9.** To a solution of monoprotected diol **8b** (106 mg, 0.19 mmol), perdeuterated 1-oxyl-2,2,5,5-tetramethylpyrroline-3-carboxylic acid (spin label **5b**; 74 mg, 0.38 mmol), and 4-(dimethylamino)pyridine (46 mg, 0.38 mmol) in THF (5 mL) was added *N,N'*-dicyclohexylcarbodiimide (78 mg, 0.38 mmol). The reaction mixture was stirred at room temperature for 3 d. The precipitate was filtered off and washed with THF. The solvent of the filtrate was removed. In order to get rid of trapped THF, the crude product was dissolved in CH<sub>2</sub>Cl<sub>2</sub> and the solvent was removed. The residue was dissolved in a small amount of CH<sub>2</sub>Cl<sub>2</sub> and the solution was applied to a chromatotron plate (thickness: 2 mm) for centrifugal chromatography. Elution with pentane/CH<sub>2</sub>Cl<sub>2</sub> 1:1 provided first a pale yellow solid (23 mg) containing nitroxide **9** and alkyne dimer **10** in a ratio of ca. 11:1 (determined through <sup>1</sup>H NMR spectroscopy) and then nitroxide **9** (104 mg, 74%) as a yellow solid. Nitroxide **9** was freeze-dried using benzene. M.p: 105-107 °C. <sup>1</sup>H NMR (250 MHz, CD<sub>2</sub>Cl<sub>2</sub>): All signals are broadened and structureless. δ = 7.60 (br s, 2 H, H meta to ester group), 7.47 (apparent d, *J* = 8.5 Hz, 2 H, H meta to OTHP), 7.38 and 7.37 (2 s, 1 H each, H ortho to Hex), 7.20 (very broad s, integration not reliably possible because of broadness and overlap with other signals, H ortho to ester group), 7.05 (apparent d, *J* = 8.4 Hz, 2 H, H ortho to OTHP), 5.45 (t, *J* = 2.9 Hz, 1 H, O<sub>2</sub>CH), 3.88 and 3.61 (2 m, 1 H each, OCH<sub>2</sub>), 2.82 (m, 4 H, ArCH<sub>2</sub>), 2.1-1.2 (m, 25 H; expected: 22 H, CH<sub>2</sub>), 0.89 (m, 6 H, CH<sub>2</sub>CH<sub>3</sub>). Elemental analysis calcd (%) for C<sub>48</sub>H<sub>45</sub>D<sub>13</sub>O<sub>5</sub>N (742.072): C 77.69, H 6.11, D 3.53, N 1.89; found C 77.61, N 1.90; Comment: with the instrument available to us, the content of H cannot be determined in the presence of D.

**Nitroxide 2.** To a solution of nitroxide **9** (93 g, 0.13 mmol) in THF (15 mL) and MeOH (5 mL) was added *p*-toluenesulfonic acid monohydrate (25 mg, 0.13 mmol). The reaction was monitored with thin layer chromatography (CH<sub>2</sub>Cl<sub>2</sub>). After 4.2 h at room temperature, Et<sub>2</sub>O and water were added. The aqueous phase was extracted with Et<sub>2</sub>O, the combined organic phases were washed with an aqueous solution of K<sub>2</sub>CO<sub>3</sub>, then aqueous 1 N HCl, and finally brine. After drying with MgSO<sub>4</sub> the solvents were removed. Centrifugal chromatography (plate thickness: 1 mm; CH<sub>2</sub>Cl<sub>2</sub>) yielded diol **8a** (4 mg; *R*<sub>f</sub> = 0.30) as a colorless solid and, as a later eluted fraction, nitroxide **2** (55 mg, 67%; *R*<sub>f</sub> = 0.34) as a yellow-redish solid. Surprisingly, diol **8a** was eluted ahead of nitroxide **2** although the *R*<sub>f</sub> values let expect them to be eluted in the reverse order. Nitroxide **2** was freeze-dried using benzene. M.p: 130-132 °C. <sup>1</sup>H NMR (250 MHz, CD<sub>2</sub>Cl<sub>2</sub>): All signals are broadened and structureless. δ = 7.60 (br s, 2 H, H meta to ester group), 7.46 (br s, 2 H, H meta to OH), 7.38 and 7.36 (2 s, 1 H each, H ortho to Hex), 7.21 (very broad s with shoulder at

6.9 ppm, integration not reliably possible because of broadness and overlap with other signals, H ortho to ester group and H ortho to OH), 2.82 (m, 4 H, ArCH<sub>2</sub>), 1.71 (m, 4 H, ArCH<sub>2</sub>CH<sub>2</sub>), 1.36 (m, about 13 H, expected: 12 H, CH<sub>2</sub>), 0.89 (m, 6 H, CH<sub>2</sub>CH<sub>3</sub>). Comment: the <sup>1</sup>H NMR signals of the protons ortho and meta to the OH group are substantially broadened in comparison to the signals of the corresponding protons of nitroxide **9**. This is thought to be caused by hydrogen bonding between the phenol moiety and the nitroxide moiety and therefore a strong effect of the paramagnetic moiety on the relaxation of these protons. Elemental analysis calcd (%) for C<sub>43</sub>H<sub>37</sub>D<sub>13</sub>O<sub>4</sub>N (657.954): C 78.50, H 5.67, D 3.98, N 2.13; found C 78.36, N 2.10; Comment: with the instrument available to us, the content of H cannot be determined in the presence of D.

#### 1.4 <sup>1</sup>H NMR spectra of nitroxides **1**, **2** and **9**

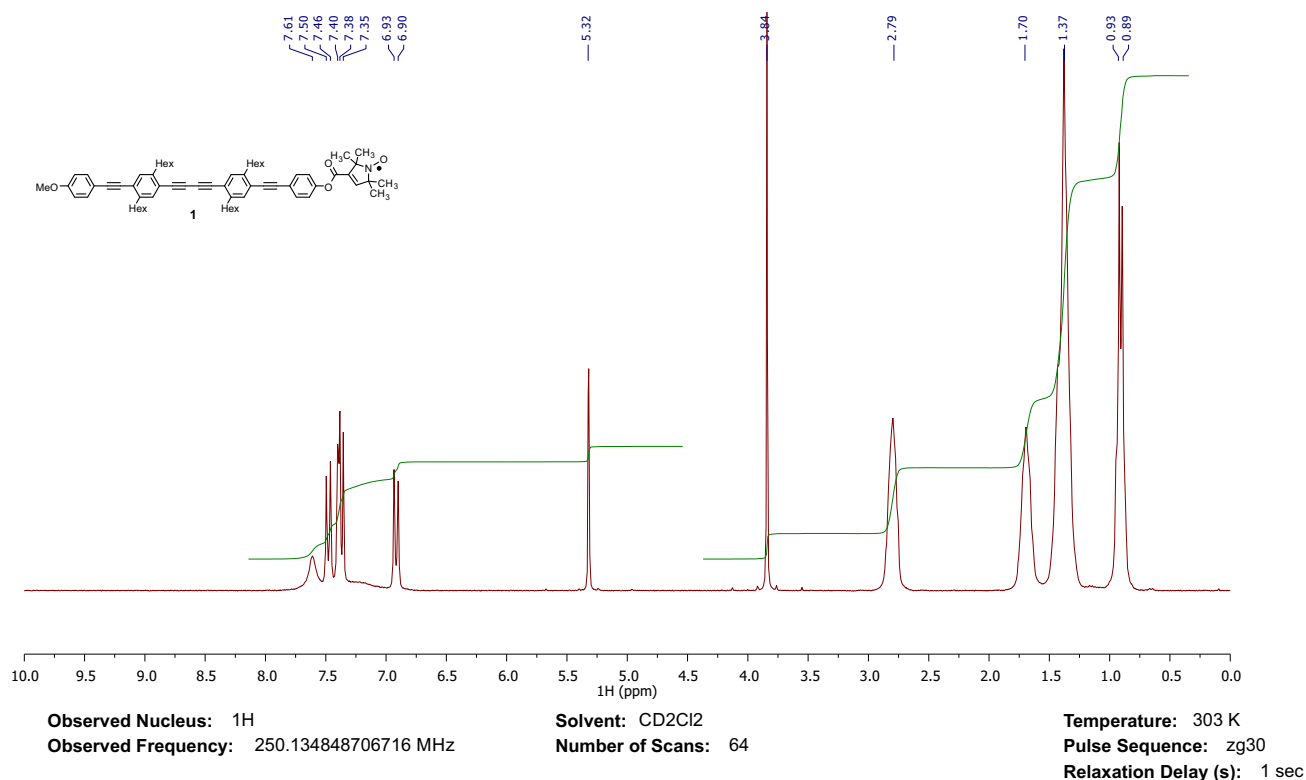


**Fig. S2.** <sup>1</sup>H NMR spectrum (250 MHz, CD<sub>2</sub>Cl<sub>2</sub>) of nitroxide **1**.

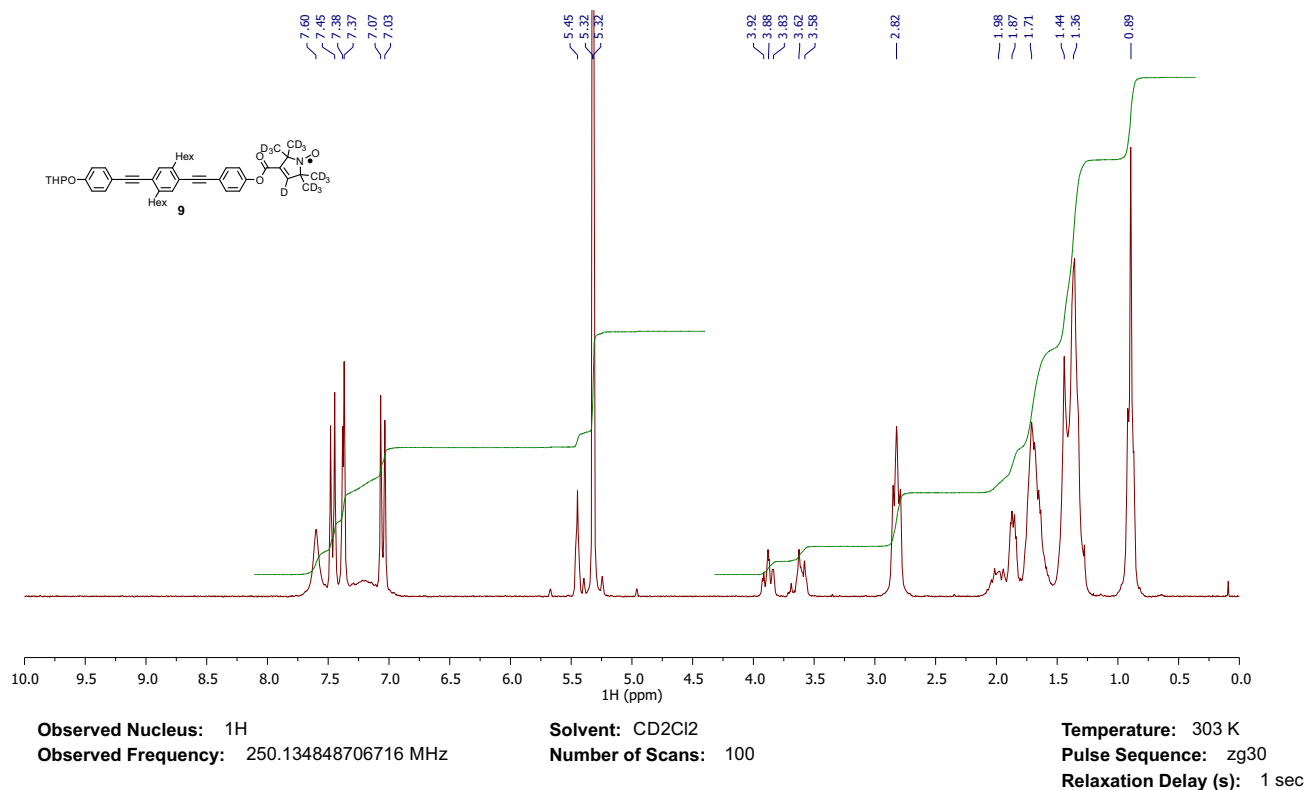


**Fig. S3.** <sup>1</sup>H NMR spectrum (250 MHz, CD<sub>2</sub>Cl<sub>2</sub>) of nitroxide **9**.

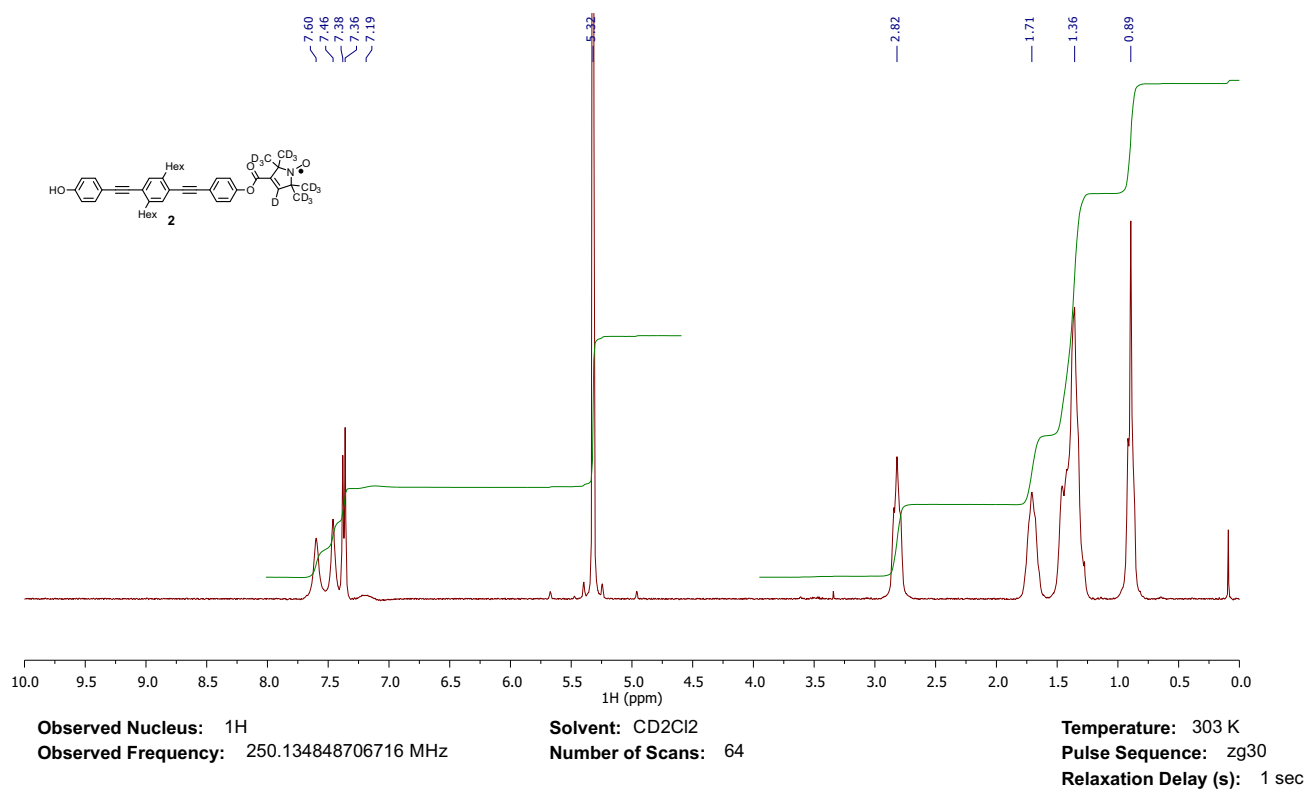


**Fig. S4.** <sup>1</sup>H NMR spectrum (250 MHz, CD<sub>2</sub>Cl<sub>2</sub>) of nitroxide **2**.

## 2 Overlapping echoes in DD sequences

Both DD experiments, CPDD and UDD, generate unintended coherence pathways due to the limited excitation bandwidth of monochromatic, rectangular pulses with respect to the Q-band nitroxide spectrum. Already for two refocusing pulses, *i.e.*  $n = 2$ , a stimulated echo overlaps at the refocusing time of the desired echo. With increasing number of  $\pi$  refocusing pulses, the number of unwanted stimulated, primary and refocused echoes increases even further. In Fig. S5 the case for  $n = 3$  for the CPDD3 experiment is illustrated.

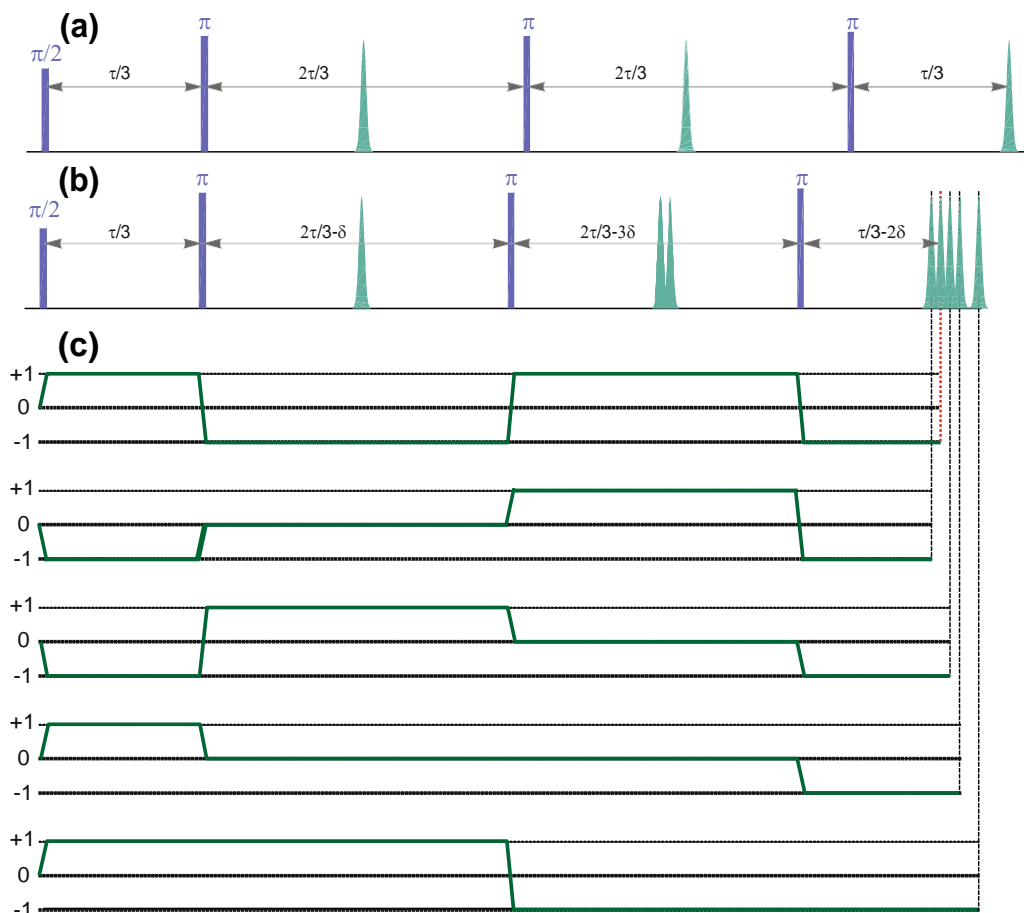


**Fig. S5.** Overlapping echoes in dynamical decoupling scheme prohibiting reliable measurement of electron spin coherence decay, here illustrated for  $n = 3$  (CPDD3).

**(a)** Standard CPDD  $n = 3$  experiment with five echoes overlapping at the observer position. **(b)** Introducing a small time shift  $\delta$  allow for full separation of all echoes. **(c)** Illustration of coherence pathways leading to all spin echoes shown in **(b)**. The first pathway leads to the wanted  $n = 3$  echo, marked by a read line.

For reliable electron spin coherence decay measurements two approaches are possible. Either an elaborate phase cycle has to be employed where each pulse, except the last  $\pi$  pulse, is cycled systematically in phase. The length of the phase cycle increases exponentially with  $n$ , hence this approach is limited. Alternatively, the interpulse delays  $\Delta_j$  have to be slightly shifted in time to allow for selection of the desired coherence pathway. In the latter case, care has to be taken to choose the time shift  $\delta$  small with respect to the interpulse delay in order to maintain the decoupling condition. In contrast to CP decoupling, Uhrig-type interpulse delays differ in length. This simplifies both the necessary phase cycle as well as the time shifting scheme. Note that the time shifting approach also leads to less apparent nuclear modulation, in particular for large ESEEM amplitudes this introduces an additional, apparent relaxation component and the phase

cycle approach should be chosen instead.

Tab S1 summarizes the timings for a DD sequence with  $n$  refocusing pulses for both CP and Uhrig decoupling. CPDD sequences require  $n - 1$  shifted interpulse delays and an appropriately shifted delay  $\Delta_{n+1}$  between the last refocusing pulse and the echo. To compute  $\Delta_{n+1}$ , the  $n - 1$  interpulse delay shifts have to be added with appropriate sign factor with  $+1$  for the shift of delay  $\Delta_n$ ,  $-1$  for the shift of delay  $\Delta_{n-1}$ , and so on with alternating signs. CPDD shifts obey the formula  $\Delta_i = i(i - 1)\frac{\delta}{2}$  starting at  $i = 2$ . UDD sequences require  $n - 2$  shifted interpulse delays and an appropriately shifted delay  $\Delta_{n+1}$  between the last refocusing pulse and the echo. Computation of  $\Delta_{n+1}$  is analogous. UDD shifts obey the formula  $\Delta_i = (i - 2)\frac{\delta}{2}$  starting at  $i = 3$ . Below a certain minimum delay  $\tau_{\min}$ , delay-dependent moving echoes may still cross the observer echo. By identifying the pathway that leads to the last crossing of the observer echo by an unwanted echo on incrementing  $\tau$ ,  $\tau_{\min}$  was determined. Applying the introduced time shift allows placing the unwanted echo at time  $\delta$  before the observer echo.

The basic phase cycle  $[(+)(+x)-(-x)]$  on the first  $(\pi/2)$  pulse is applied in both approaches in order to enforce coherence generation of this pulse and cancel a receiver offset. For a full phase cycle,  $\delta = 0$  can be applied and the  $\tau_{\min}$  is, in principle, only determined by the spectrometer dead time. In the full phase cycle, the last refocusing pulse with index  $n$  does not need to be cycled in phase, while pulse  $n - 1$  (for  $n > 1$ ) is subjected to a phase cycle  $[(+)(+x)+(-x)]$  to suppress transfer to polarization. All remaining refocusing pulses (for  $n > 2$ ) are subjected to a phase cycle  $[(+)(+x)-(-y)+(+x)-(-y)]$  to enforce inversion of coherence order. Accordingly, full phase cycles have 2 steps for  $n = 1$  and  $4^{n-1}$  for  $n > 1$ .

The Matlab scripts used to compute the echo timings, coherence transfer pathways, and influence of phase cycling and to produce Figure S5 are provided as Supplementary Material. Briefly, the computations are based on a two-level system with coherence orders  $p = +1$ , corresponding to the  $\hat{S}^+$  element of the density operator  $\sigma$ ,  $p = 0$  for polarization corresponding to the diagonal elements of  $\sigma$ , and  $p = -1$ , corresponding to the  $\hat{S}^-$  element of  $\sigma$ . Function `echo_pathways` generates all coherence transfer pathways starting from  $p = 0$  before the first pulse and determines which pathways are consistent with the specified phase cycles of all pulses. For these allowed pathways, function `compute_echoes` computes times of refocusing by the condition  $\sum_i t_i p_i = 0$ , where  $i$  runs over all time delays between pulses, including the time after the last pulse. Note that for a single coherence transfer pathway the refocusing condition can be fulfilled several times. An echo occurs if, at a time of refocusing, the coherence order is  $p = -1$ . A single pathway may give rise to more than one echo.

Function `plot_sequence` plots the specified pulse sequence with pulses denote by pale blue vertical rectangles and labelled by there number and delays denoted by red horizontal bars and also labelled by their number. Clicking on a vertical blue bar causes the pulse to light up yellow for a short time and displays information on pulse timing, pulse length, increment of the pulse time, and phase cycle in the Matlab command window. Clicking in a horizontal red bar causes this bar to light up shortly and displays the initial starting time of the delay, the initial delay length, the starting time increment, and the delay length increment in the Matlab comman window.

Function `plot_echoes` displays the echoes as semi-transparent green Gaussian shapes. Due to the transparency, one can judge whether two or more echoes coincide in time. In such a case, the echo appears darker. Note that echo phase is ignored. All echoes are plotted positive, whereas some of them might be negative or dispersive in the experiment. Clicking on an echo causes the echo to light up shortly in yellow and to become colored orange afterwards. Only the last clicked echo is displayed in orange color. Timing of the echo is displayed in the Matlab command window and a graphical representation of the coherence order pathway leading to this echo is added to the figure.

The figure features an `Animate` button in the lower left corner. When this button is clicked, all delays are incremented step by step for the total number of data points specified by the user. Pulse and echo times are recomputed and the figure is updated for each data point. The orange color

of the last clicked echo makes it easier to see whether this echo is crossed by other echoes during incrementation.

All functions are called by the script `example_echo_computer`. This commented script also explains how to specify pulse, phase cycling, delays, increments, and the number of data points. Pulses with coupled phase cycles must have the same length and must be specified by the same pulse index. Incoherent pulses can be specified by replacing the phase cycle by the negative imaginary unit  $-1i$ , but an also be simply omitted. The functions are part of the more general pulse sequence specification and simulation software PUSH (Pulse Sequence Helper), which will be published elsewhere.

**Table S1** Delays and delay shifts for CP and Uhrig type decoupling experiments as a function of number of refocusing pulses  $n$  for a total sequence length of  $2\tau$ . The  $\Delta_1, \dots, \Delta_n$  interpulse delays are placed before each refocusing pulse, so that  $\Delta_{n+1}$  marks the time between the last refocusing pulse and the echo position. For a full phase cycle the time shift  $\delta$  can be set to zero. In all other cases,  $\delta$  allows separation of the unwanted echo from the observer echo by implementing  $\tau > \tau_{\min}$  and applying a  $[+(+x)-(-x)]$  phase cycle on the first  $\pi/2$  pulse.

Sequence	$n$	$\Delta_1$	$\Delta_2$	$\Delta_3$	$\Delta_4$	$\Delta_5$	$\Delta_6$
Hahn	1	$\tau$	$\tau$	-	-	-	-
CPDD2	2	$\frac{\tau}{2}$	$\tau + \delta$	$\frac{\tau}{2} + \delta$	-	-	-
CPDD3	3	$\frac{\tau}{3}$	$\frac{2\tau}{3} + \delta$	$\frac{2\tau}{3} + 3\delta$	$\frac{\tau}{3} + 2\delta$	-	-
CPDD4	4	$\frac{\tau}{4}$	$\frac{\tau}{2} + \delta$	$\frac{\tau}{2} + 3\delta$	$\frac{\tau}{2} + 6\delta$	$\frac{\tau}{4} + 4\delta$	-
CPDD5	5	$\frac{\tau}{5}$	$\frac{2\tau}{5} + \delta$	$\frac{2\tau}{5} + 3\delta$	$\frac{2\tau}{5} + 6\delta$	$\frac{2\tau}{5} + 8\delta$	$\tau/5 + 6\delta$
UDD3	3	$(1 - \frac{1}{\sqrt{2}})\tau$	$\frac{\tau}{\sqrt{2}}$	$\frac{\tau}{\sqrt{2}} + \delta$	$(1 - \frac{1}{\sqrt{2}})\tau + \delta$	-	-
UDD4	4	$(3 - \sqrt{5})\frac{\tau}{4}$	$\frac{\tau}{2}$	$(\sqrt{5} - 1)\frac{\tau}{2} + \delta$	$\frac{\tau}{2} + 2\delta$	$(3 - \sqrt{5})\frac{\tau}{4} + \delta$	-
UDD5	5	$(2 - \sqrt{3})\frac{\tau}{2}$	$(\sqrt{3} - 1)\frac{\tau}{2}$	$\frac{\tau}{2} + \delta$	$\frac{\tau}{2} + 2\delta$	$(\sqrt{3} - 1)\frac{\tau}{2} + 3\delta$	$(2 - \sqrt{3})\frac{\tau}{2} + 2\delta$

### 3 Fitting procedure for Hahn echo and DD relaxation traces

Experimental data was fitted by either an SE or SSE model, as defined in the main text, by using the non-linear least squared approach. Upper boundary conditions as well as initial parameter values were estimated from characteristics of the decay curve. *I.e.*  $T_{m_2, \text{initial}}$  was based on the time at which the initial echo intensity  $I_0$  has decayed to a level  $I_0/e$  and  $T_{m_1}$  was initialized based on  $T_{m_1, \text{initial}} = 0.1 \cdot T_{m_2, \text{initial}}$ . For relaxation traces with noticeable ESEEM modulation, the data was first subjected to a peak picking routine. Subsequently only the maxima of the modulation served as input data to the fitting algorithm<sup>?</sup> (see Fig. 3 (a) and (c) in the main text for illustration of representative data points within the first few microseconds of the decay trace). Equal weighing of the entire relaxation trace was ensured by maintaining this data spacing also in the time region past the pronounced ESEEM modulation. The obtained values for the fitting parameters are associated with an uncertainty due to the experimental dead time. This in turn influences the fidelity of the extrapolation to  $t = 0 \mu\text{s}$ . Note that all relaxation trace abscissae display the time elapsed after the first pulse. The associated uncertainties of the obtained fitting parameters were computed by the following procedure:

1. SSE (or SE) parameters were extracted from Hahn echo relaxation traces, handling the ESEEM modulation as described above.
2. The obtained parameters were used to generate simulated decay traces with the time axis starting at the first experimental ESEEM maximum. Fitting conditions for experimental data as described under 1. were mimicked by
  - (a) superimposing a damped cosine function (only for uncertainty bars of Hahn echo derived fit parameters<sup>†</sup>) and
  - (b) adding normally distributed pseudo-random numbers to imitate white noise at the experimentally observed signal-to-noise level (SNL)
3. The simulated decay traces were subjected to the same fitting routine to determine deviations from the known underlying input parameters.
4. The uncertainty bars presented in Fig. 5 in the main text are a direct representation of this deviation. For fitting parameters obtained from relaxation traces under DD (with  $n \geq 2$ ) in Fig. 8 in the main text, the associated uncertainties were approximated based on Hahn echo derived parameter value. In these cases the time axis matched the first ESEEM maximum of the corresponding DD relaxation traces. In this way, the influence of larger experimental dead time onto the uncertainty of the parameter values was quantified.

---

<sup>†</sup>This treatment was not applied to relaxation traces under DD due to increasingly strong nuclear modulation with each additional  $\pi$  pulse.<sup>?</sup> A superposition of amplitudes and frequencies results from the repeated distribution of electron spin coherence among forbidden transitions by each refocusing pulse.

## 4 Temperature dependent Hahn echo series

### 4.1 Experimental relaxation traces

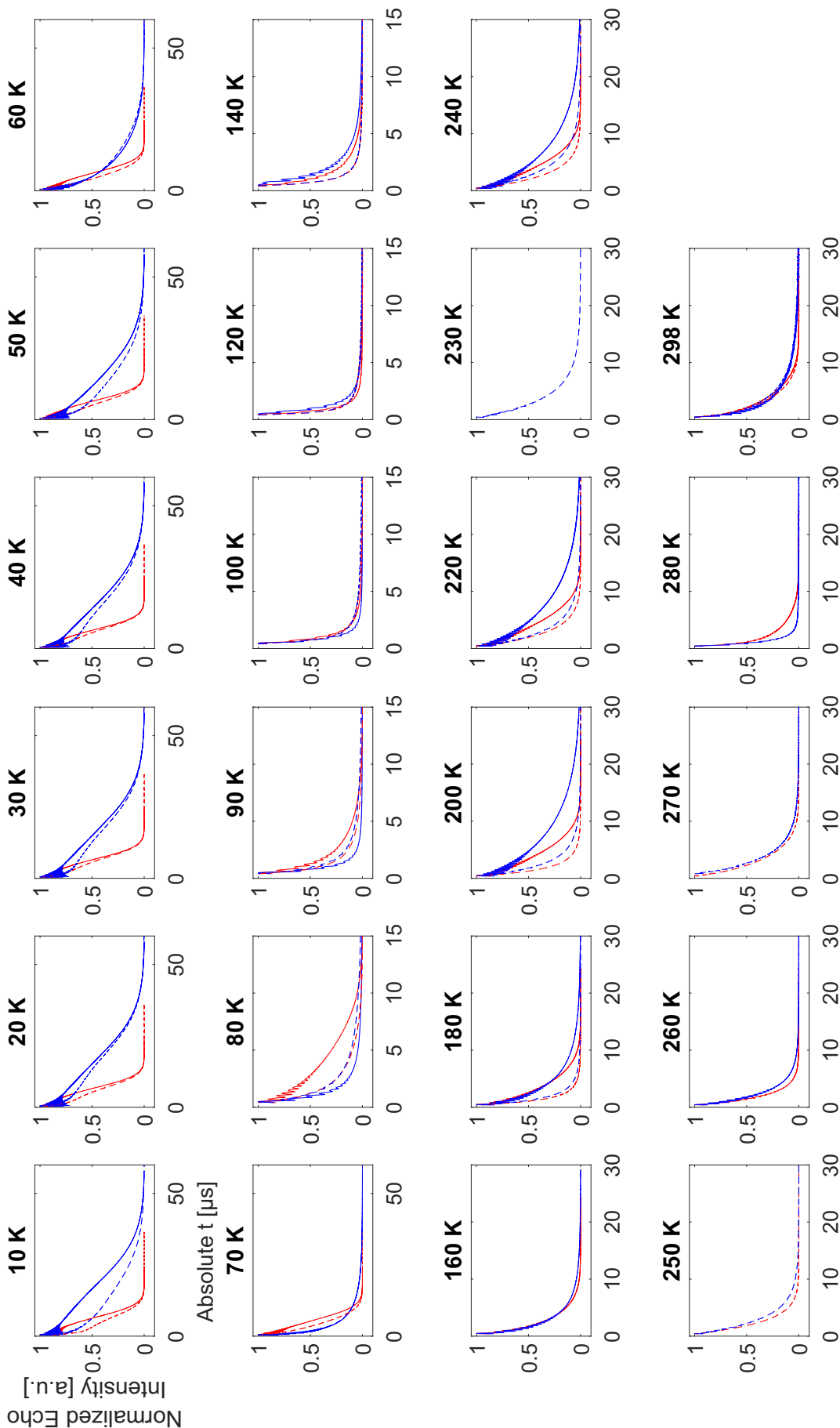


**Fig. S6.** Experimental Hahn echo relaxation traces for 100  $\mu\text{M}$  nitroxides **1** and **2** in both OTP and dOTP matrices recorded with  $t_{\pi} = 2 \cdot t_{\pi/2} = 12$  ns as a function of temperature from 10 K to room temperature. The displayed echo intensities are normalized to their respective maxima. Relaxation data in OTP matrix is displayed in red, while dOTP matrix is shown in blue. Nitroxides **1** and **2** are distinguished by dashed and solid lines, respectively. The relative echo intensities between 70 and 90 K are in particular noteworthy as the completely deuterated sample exhibits the lowest echo intensity of the four sample compositions, while complete or partial sample deuteration typically prolongs the observed phase memory time. This is discussed under section 3.2.2. in the main text.

## 4.2 Extrapolated relaxation traces

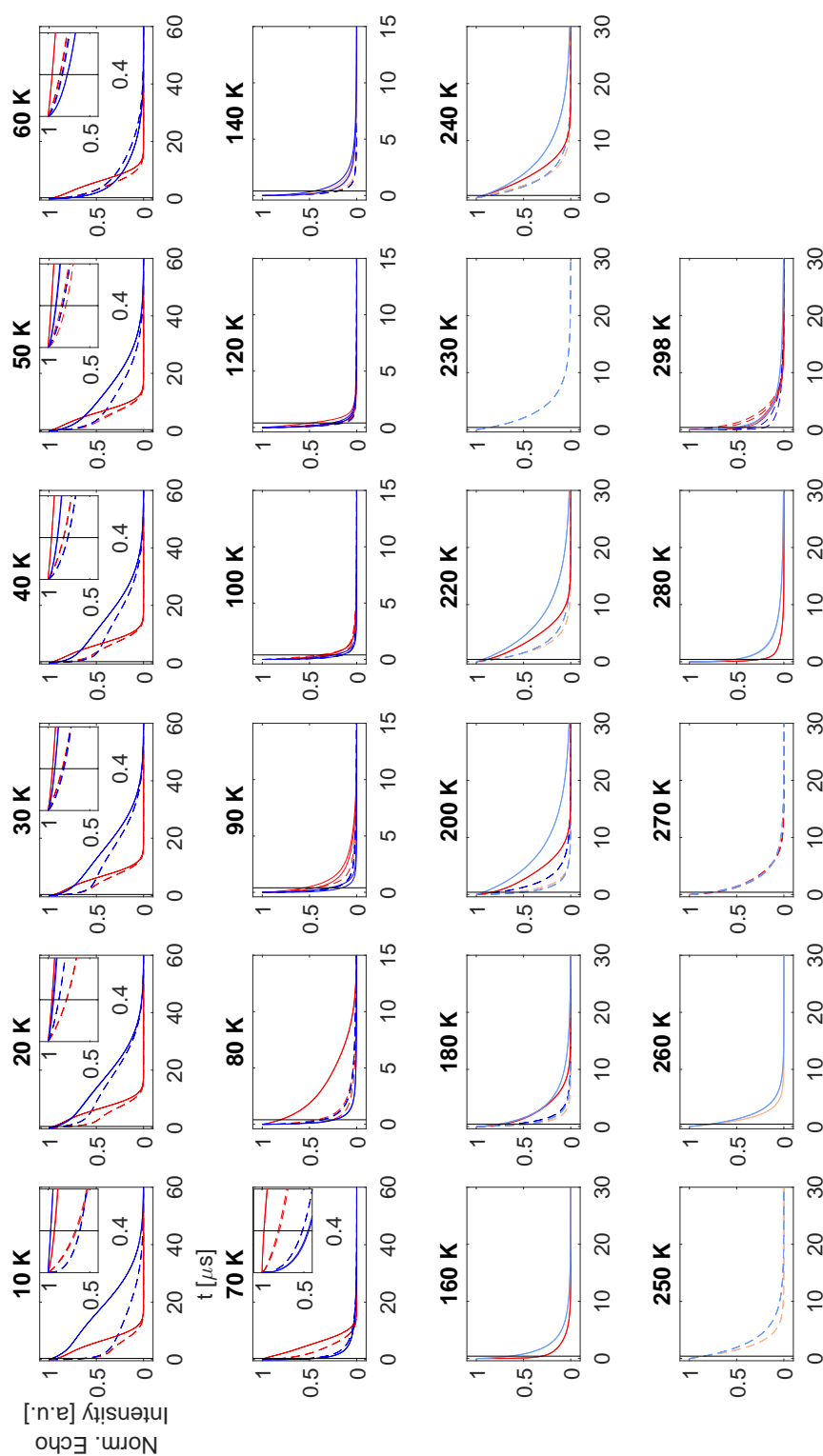


**Fig. S7.** Hahn echo relaxation traces extrapolated into the experimental dead time of 400 ns based on SSE or SE fits to the experimental figure shown in Fig. S6, to evaluate the effect of characteristic decay during the dead time as discussed under section 3.2 in the main text. Colorscheme and linetype correspond to the convention in Fig. S6, with red marking the OTP matrix and blue the dOTP matrix, while dashed and solid lines correspond to nitroxides **1** and **2**, respectively. The vertical black line marks the experimental dead time of 400 ns. For 10 to 70 K the inset shows the intensity relations for the four samples around the 400 ns. Here, the echo intensity is normalized to the time  $r(1) = 0$  ns instead of  $r(1) = 400$  ns.

### 4.3 SE vs SSE parameterization

The following section provides the Hahn echo relaxation traces for the four sample compositions at 100  $\mu\text{M}$  as a function of temperature recorded with  $t_\pi = 2 \cdot t_{\pi/2} = 12$  ns. Fig. S8 to Fig. S11 follow the same structure and are intended to provide background information to Fig. 5 in the main text and Fig. S12 in the ESI. As visible in Fig. S8 **(a)** and **(b)**, each Hahn echo relaxation trace for a specific sample composition, here nitroxide **1** in OTP, is displayed for a given temperature (in blue) together with the fit (in red) based on the SE **(a)** and SSE **(b)** model. In the latter case, the dashed black lines specify the two exponential contributions to the SSE model, while the solid black lines show the residuals. Each plot reports the underlying fitting parameters as defined in the main text, while the first vector element specifies SSE parameters  $C_i$ ,  $A_i$ ,  $T_{m_i}$  and  $\xi_i$  with  $i = 1$ . Moreover, the sum of squares (SS) are provided as an indication of the quality of fit. However due to noticeable (for nitroxide **1** in OTP) to strong (for nitroxide **2** in dOTP) ESEEM modulation, the displayed residuals allow for a more reliable and visual ranking of the two relaxation models. The title of the more appropriate model, *i.e.* resulting in flatter residuals, is highlighted for each sample composition and temperature, following a color scheme as used in Fig. 5 in the main text and Fig. S12 in the ESI: The light yellow shading corresponds to a temperature regime for which a two component expression is clearly required for *all* sample compositions as the SE model leads to strongly oscillating residuals, such as the ones shown in Fig. S8 **(a)**. In other cases, both the SE and the SSE model fit the experimental data equally to similarly well. In borderline cases the subfigure titles of both, the SSE and SE model is highlighted in blue. This observation is sample composition dependent, and occurs between 70 and 140 K, corresponding to the second temperature regime highlighted hence in blue in Fig. 5 in the main and Fig. S12 in the ESI. Between 160 K and below RT, the darker yellow temperature regime can both be described by the SE and the SSE model. However, to prevent over-parameterization by the SSE model, the simpler SE expression is used if SS value along with the residuals are similar. Sometimes, the SSE fit results in an effective SE parameterization with weighing factor  $A_1 \gg A_2$ , such as for nitroxide **2** in dOTP at 280 K as shown in Fig. S11. This is colorcoded by the light yellow shade. Note, that nitroxide **2** in OTP poses an exception as this sample composition requires an SSE parameterization, while for the other three sample compositions the SE model suffices.

## 4.3.1 Nitroxide 1 in OTP

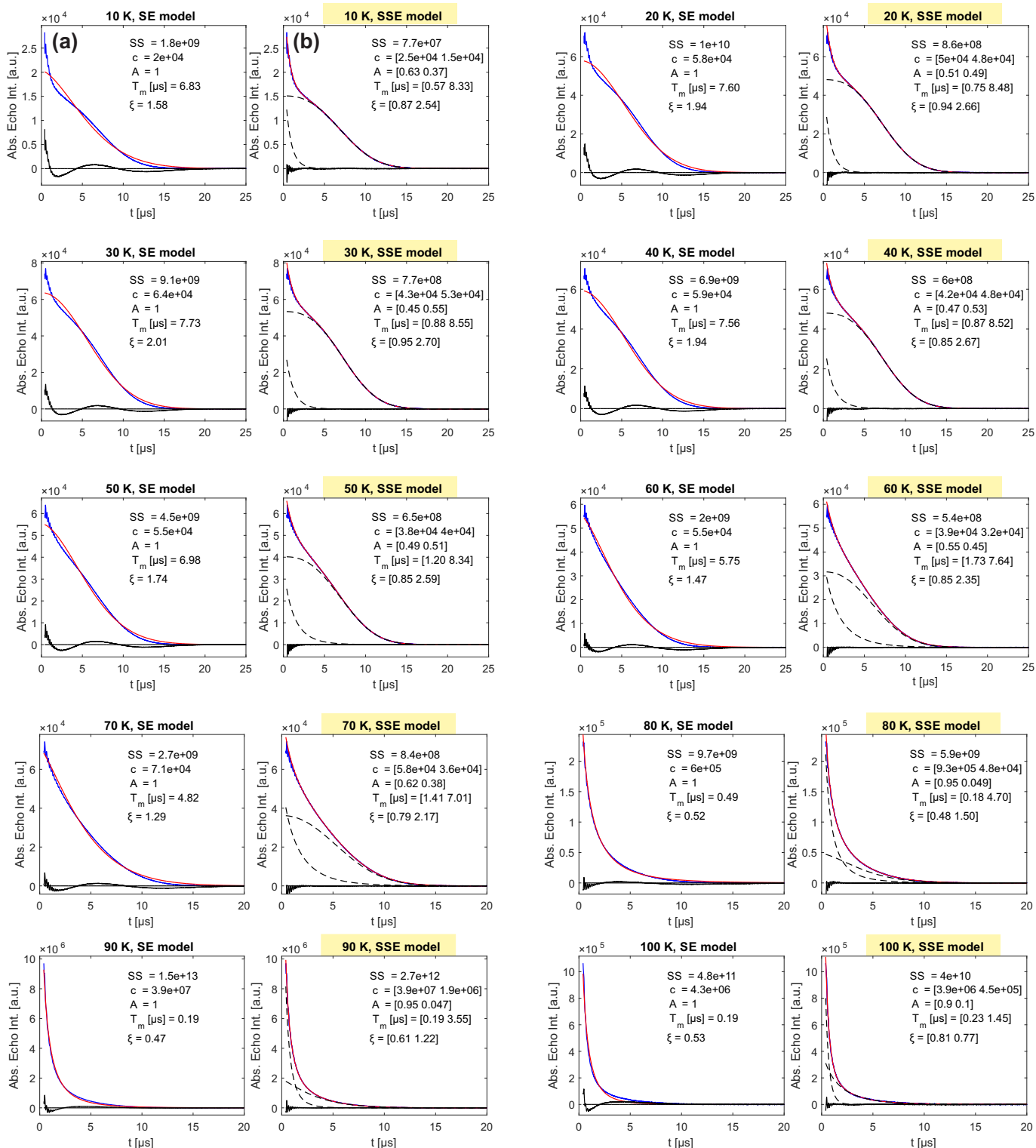


**Fig. S8.** Temperature dependent (10 K to 100 K, see next page for 120 to 298 K) Hahn echo relaxation traces recorded with  $t_\pi = 2 \cdot t_{\pi/2} = 12$  ns for 100  $\mu$ M nitroxide 1 in OTP (blue). Refer to section 4.3 for a detailed description.

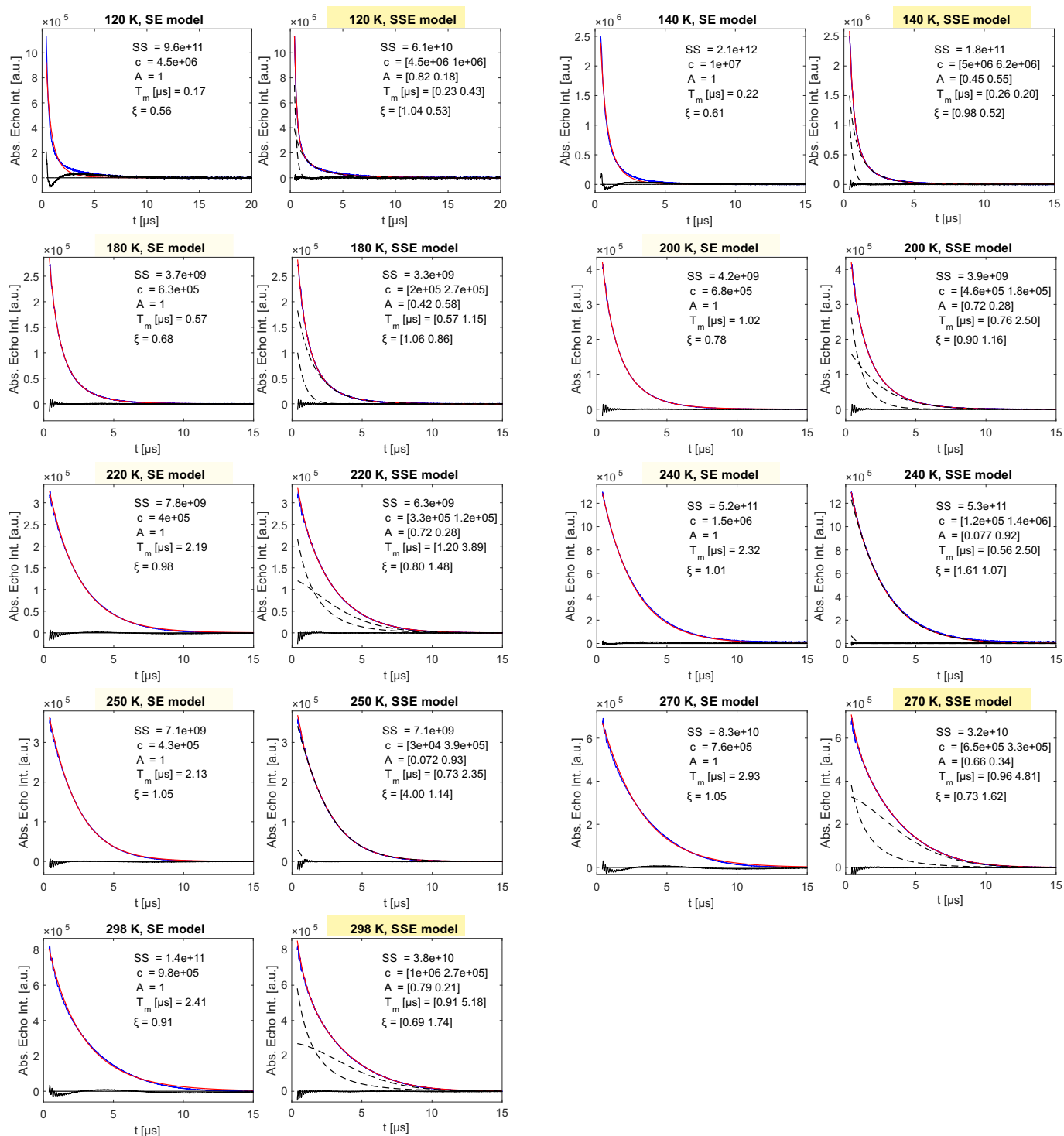


**Fig. S8.** Temperature dependent (120 K to 298 K, see previous page for 10 to 100 K) Hahn echo relaxation traces recorded with  $t_\pi = 2 \cdot t_{\pi/2} = 12$  ns for 100  $\mu\text{M}$  nitroxide **1** in OTP (blue). Refer to section 4.3 for a detailed description.

## 4.3.2 Nitroxide 1 in dOTP

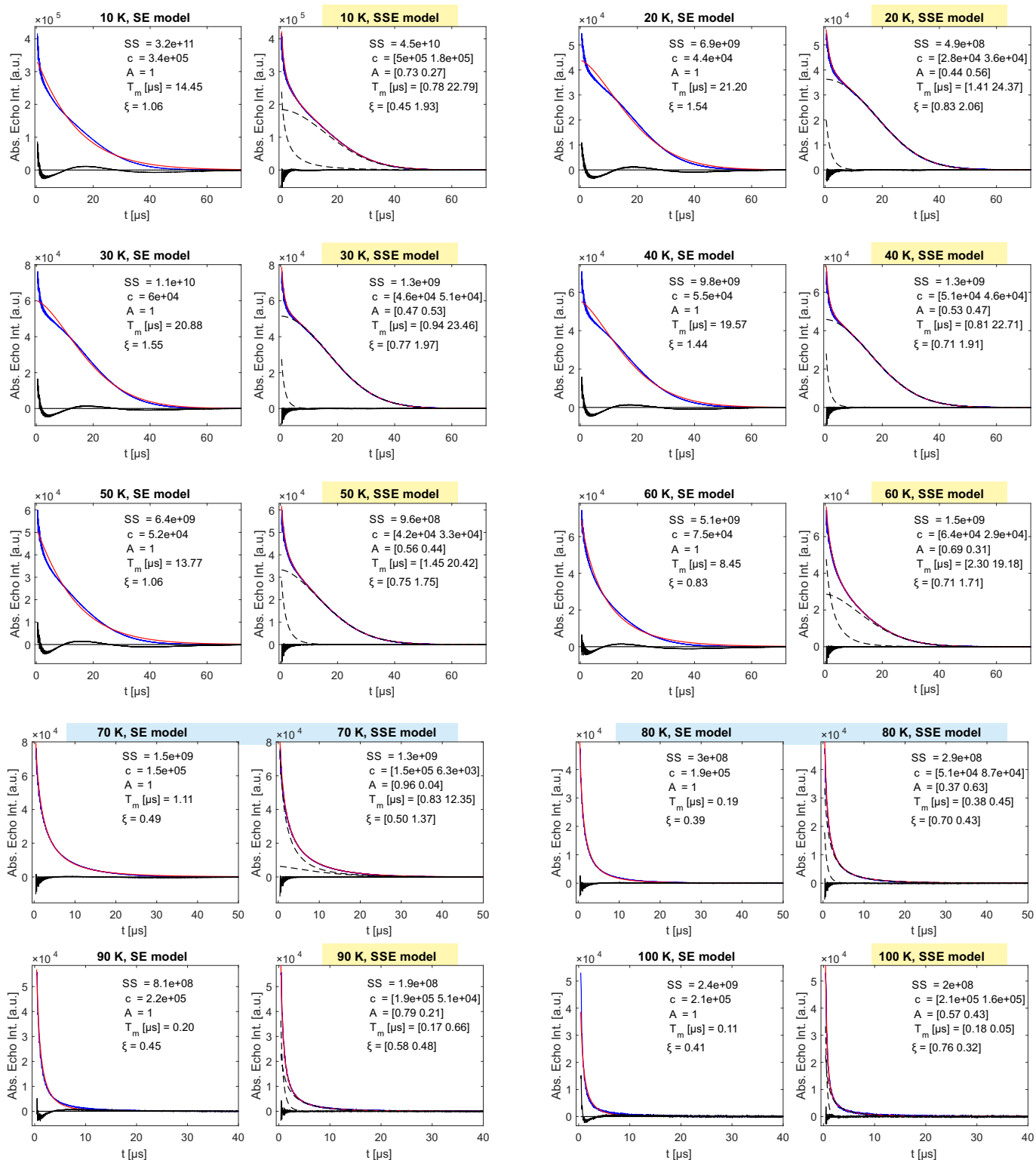


**Fig. S9.** Temperature dependent (10 K to 100 K, see next page for 120 to 298 K) Hahn echo relaxation traces recorded with  $t_\pi = 2 \cdot t_{\pi/2} = 12$  ns for 100  $\mu$ M nitroxide 1 in dOTP (blue). Refer to section 4.3 for a detailed description.

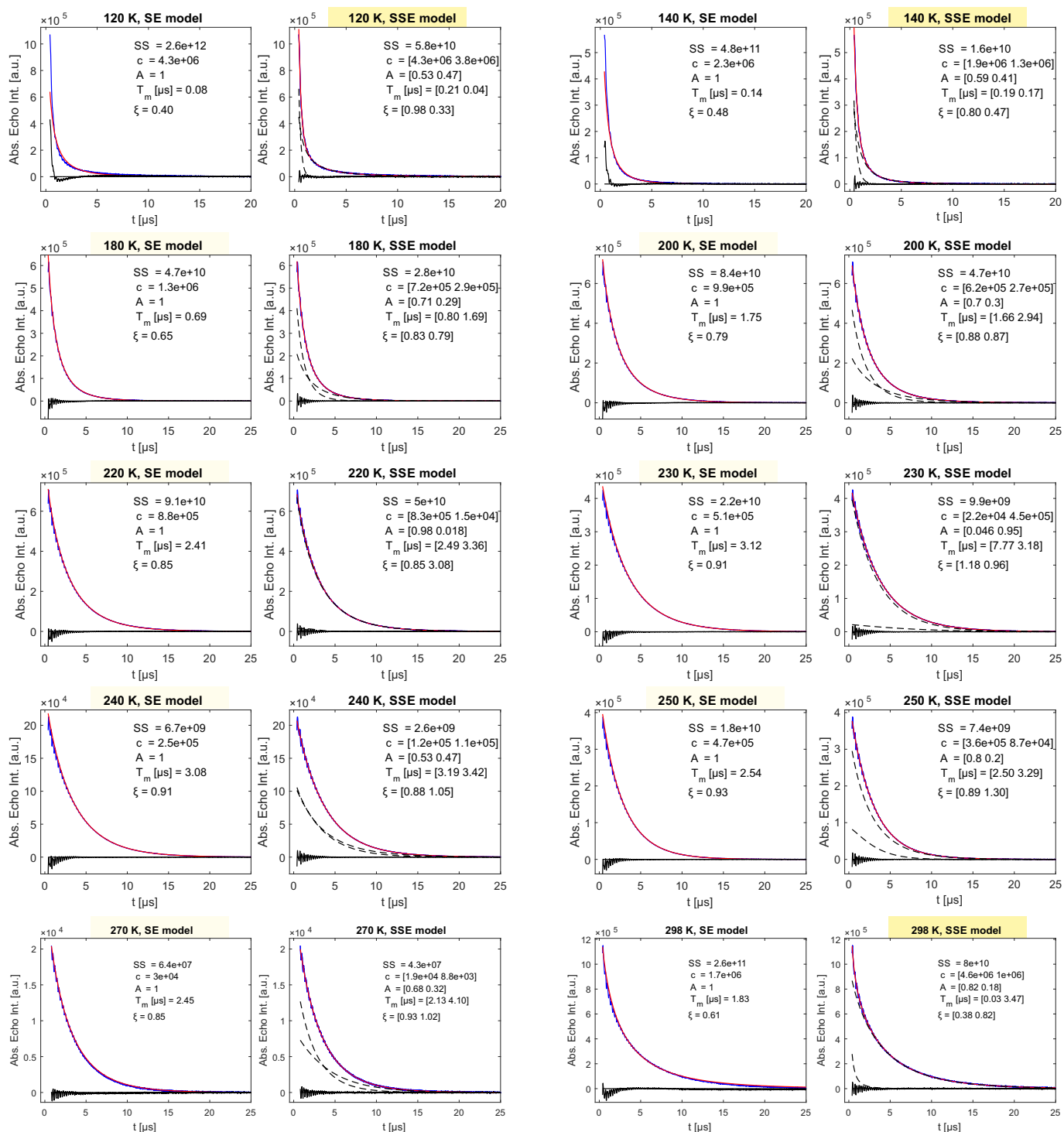


**Fig. S9.** Temperature dependent (120 K to 298 K, see previous page for 10 to 100 K) Hahn echo relaxation traces recorded with  $t_\pi = 2 \cdot t_{\pi/2} = 12$  ns for 100  $\mu\text{M}$  nitroxide **1** in dOTP (blue). Refer to section 4.3 for a detailed description.

## 4.3.3 Nitroxide 2 in OTP

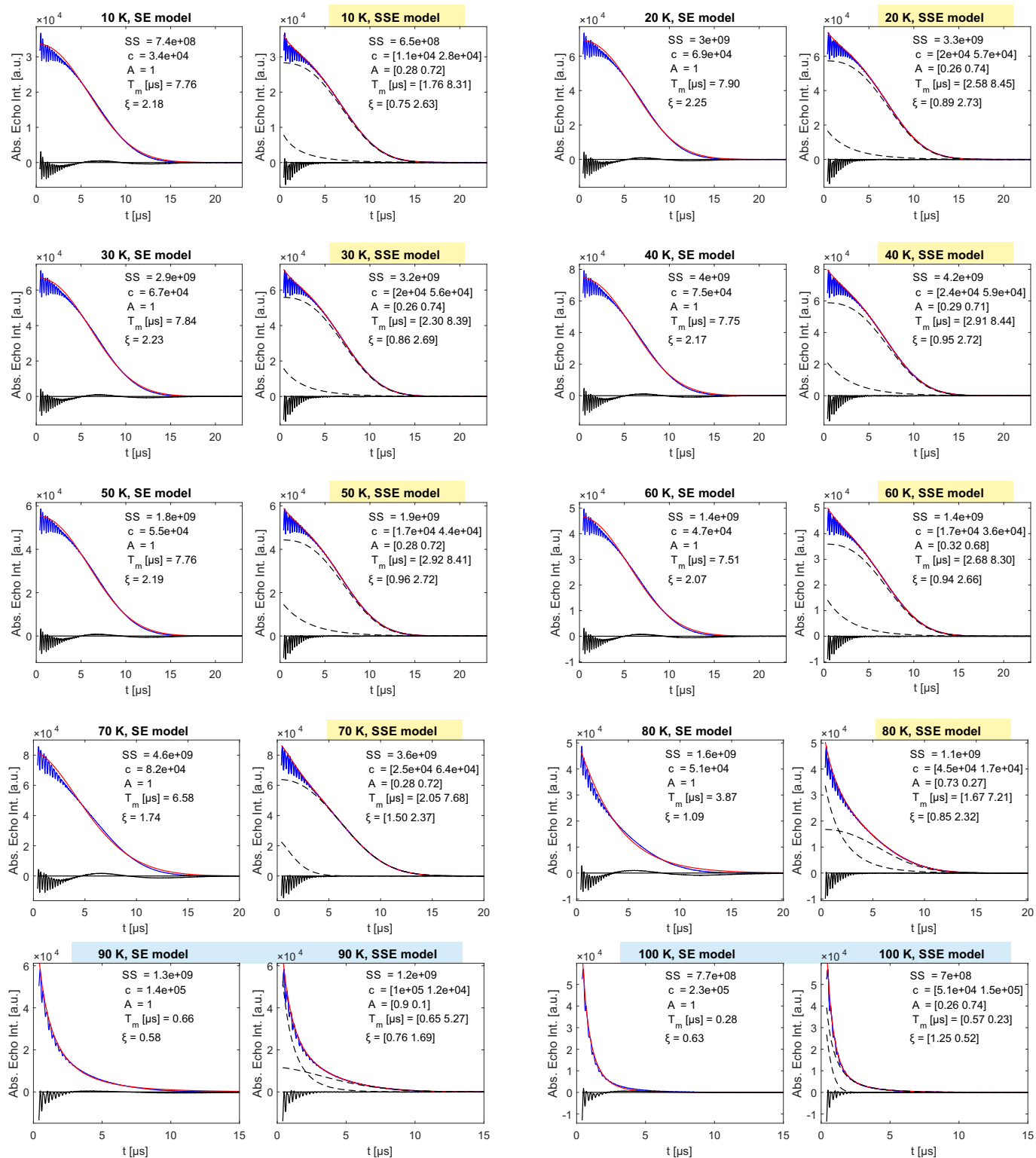


**Fig. S10.** Temperature dependent (10 K to 100 K, see next page for 120 to 298 K) Hahn echo relaxation traces recorded with  $t_\pi = 2 \cdot t_{\pi/2} = 12$  ns for 100  $\mu$ M nitroxide 2 in OTP (blue). Refer to section 4.3 for a detailed description.

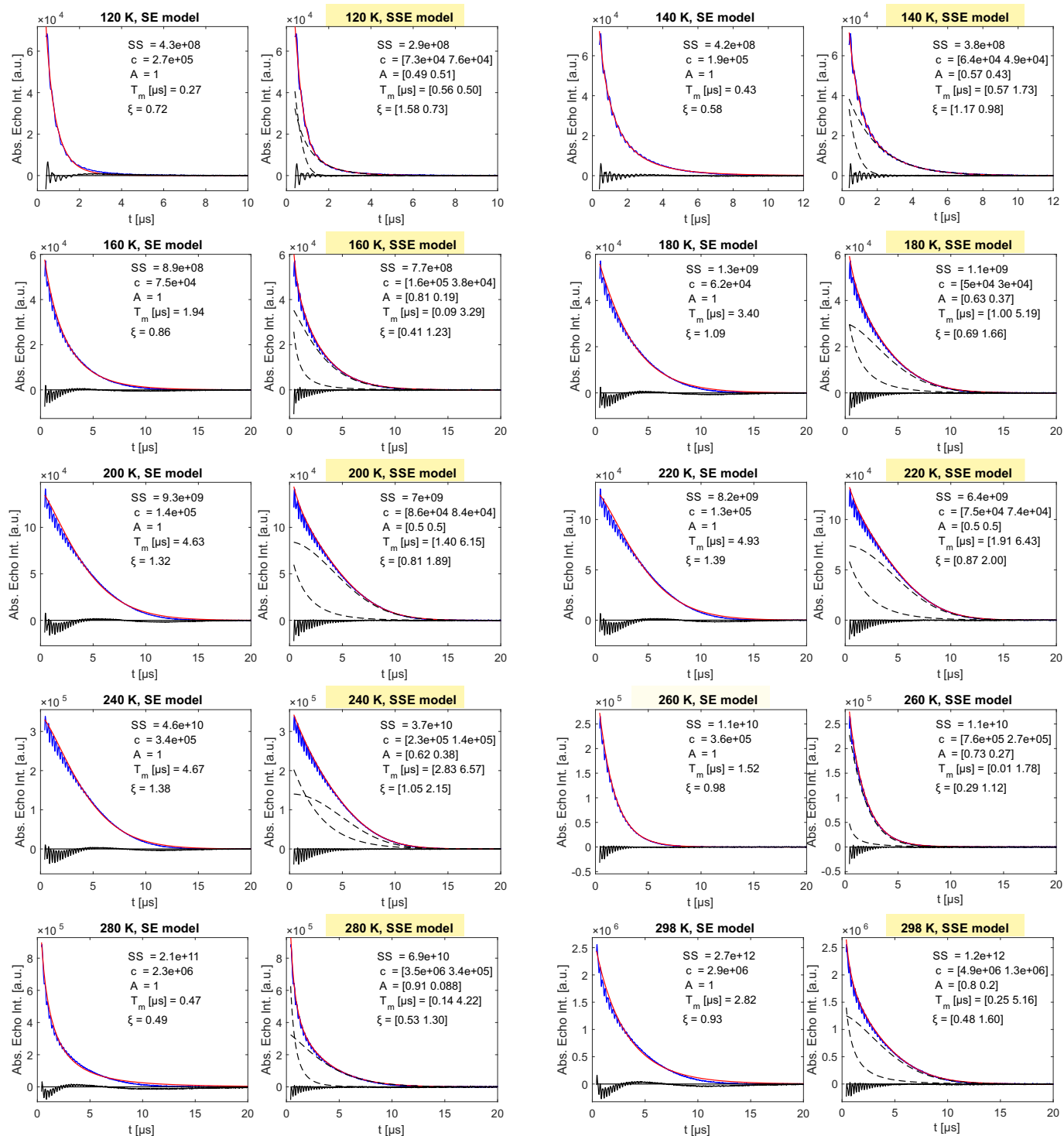


**Fig. S10.** Temperature dependent (120 K to 298 K, see previous page for 10 to 100 K) Hahn echo relaxation traces recorded with  $t_\pi = 2 \cdot t_{\pi/2} = 12$  ns for 100  $\mu$ M nitroxide **2** in OTP (blue). Refer to section 4.3 for a detailed description.

## 4.3.4 Nitroxide 2 in dOTP

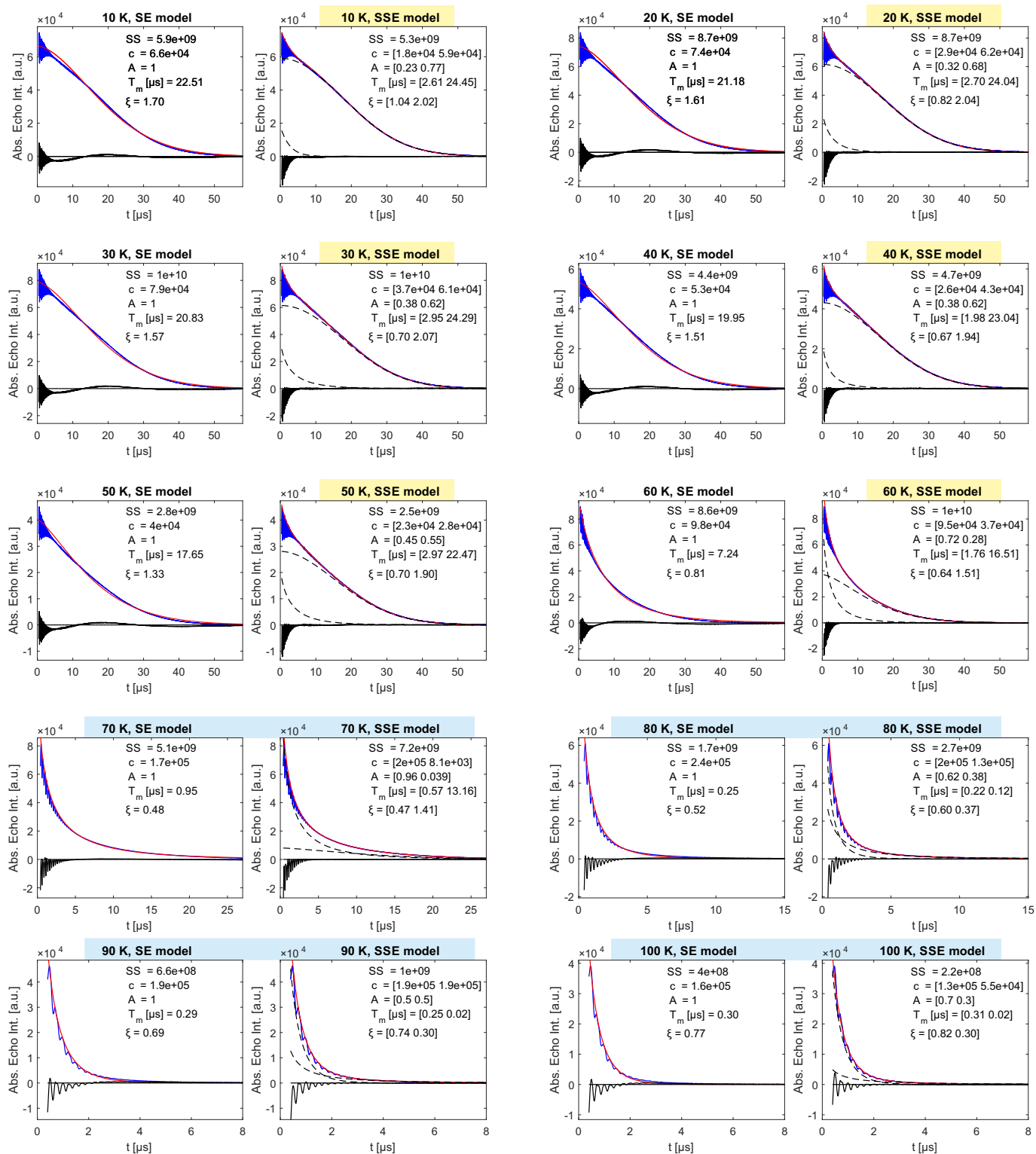


**Fig. S11.** Temperature dependent (10 K to 100 K, see next page for 120 to 298 K) Hahn echo relaxation traces recorded with  $t_\pi = 2 \cdot t_{\pi/2} = 12$  ns for 100  $\mu$ M nitroxide 2 in dOTP (blue). Refer to section 4.3 for a detailed description.

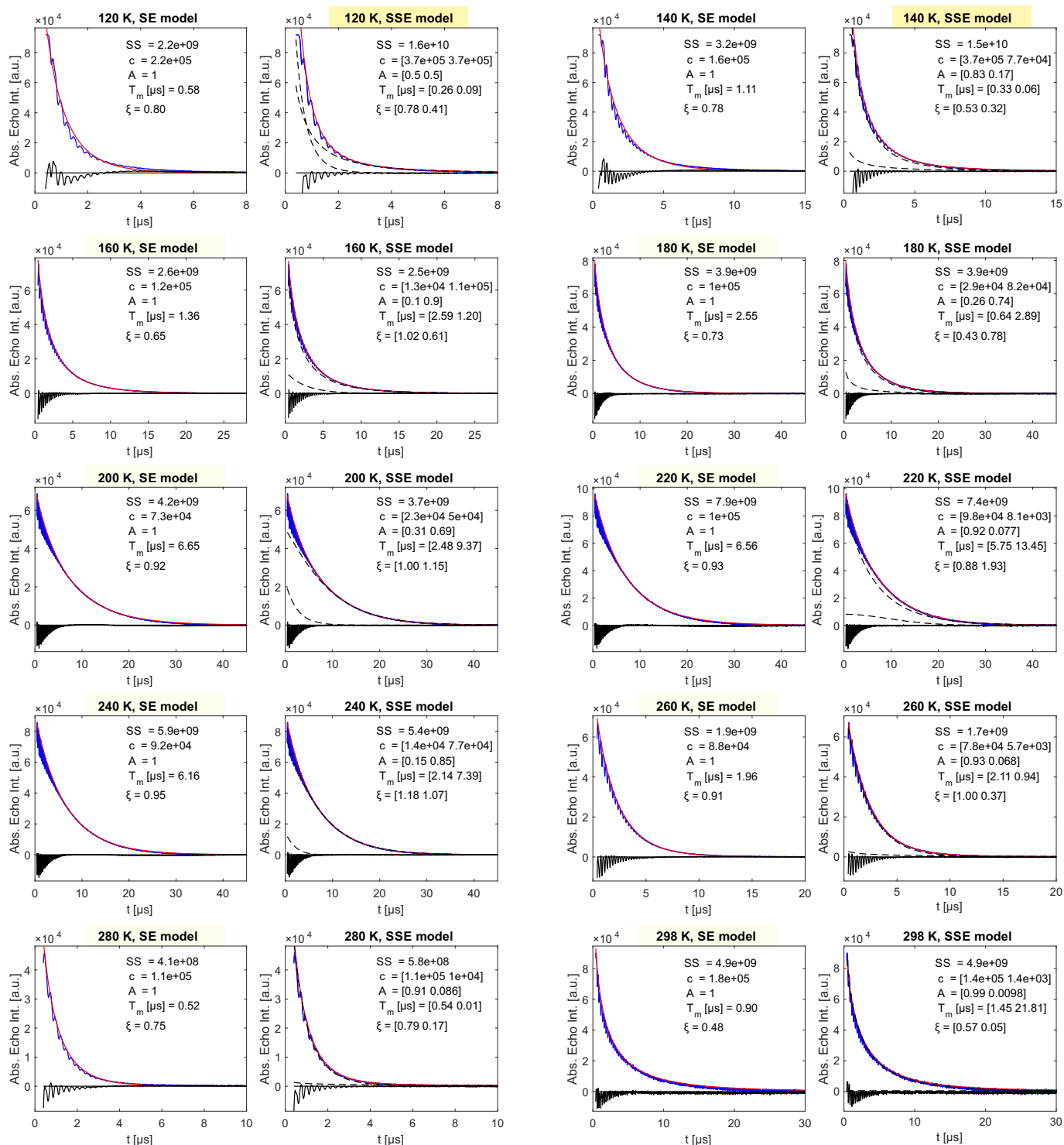


**Fig. S11.** Temperature dependent (120 K to 298 K, see previous page for 10 to 100 K) Hahn echo relaxation traces recorded with  $t_\pi = 2 \cdot t_{\pi/2} = 12$  ns for 100  $\mu$ M nitroxide 2 in dOTP (blue). Refer to section 4.3 for a detailed description.

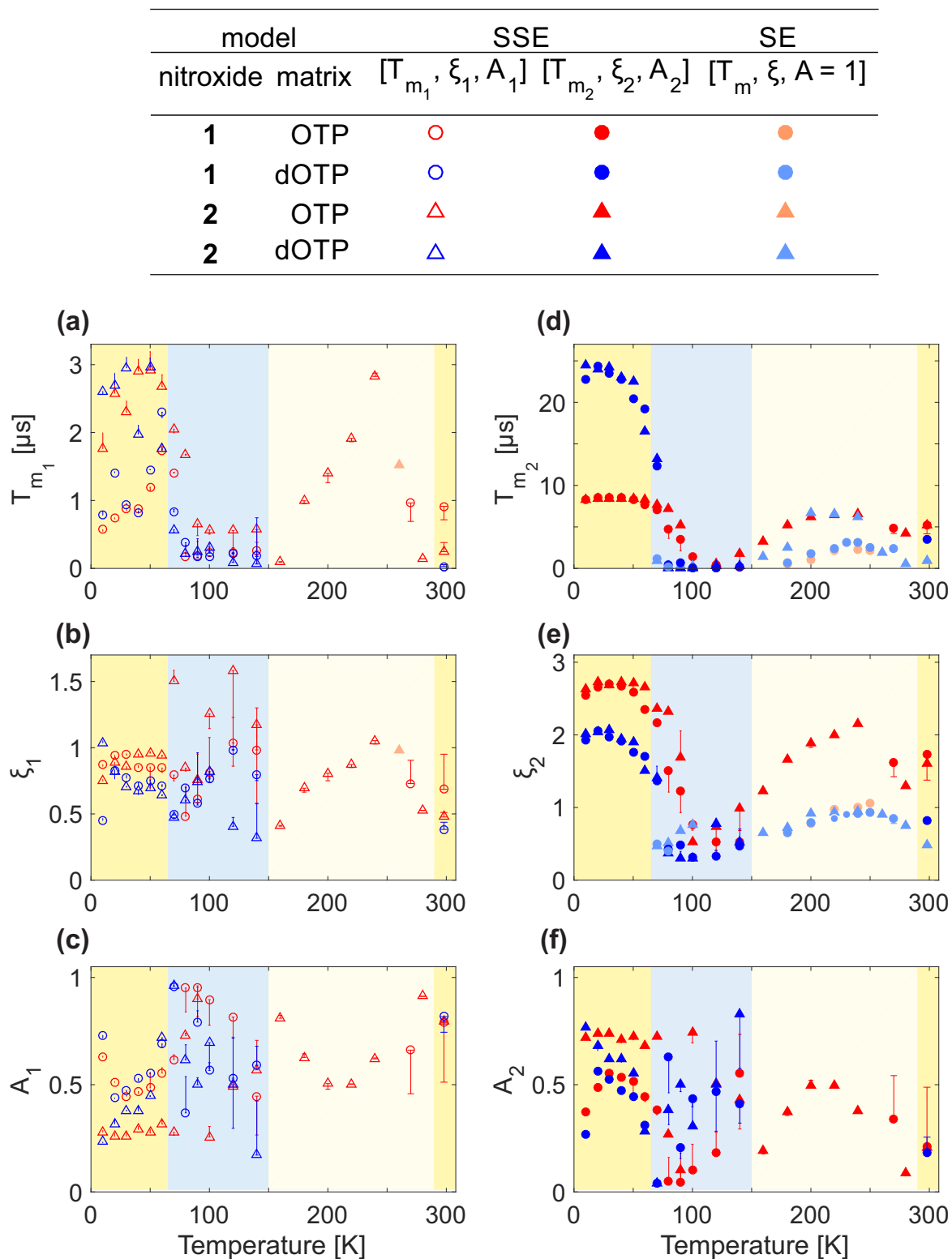


**Fig. S12.** SSE and SE parameterization of Hahn echo decay traces as a function of temperature for 100  $\mu$ M nitroxide **1** and **2** in OTP and dOTP. This figure is a more detailed representation of Fig. 5 in the main text, where the slow and fast components, *i.e.* parameters  $T_{m_i}$ ,  $\xi_i$  and  $A_i$  for  $i = 1, 2$ , are displayed separately. The top most table serves as a legend, distinguishing sample composition and fit model by maker type and color. The underlying Hahn echo relaxation curves can be found in section 4.3 for each sample composition. The shaded background indicates the temperature regimes, as discussed in the main text.

## 5 Temperature dependent ESE detected fieldsweep of nitroxide 2 in dOTP

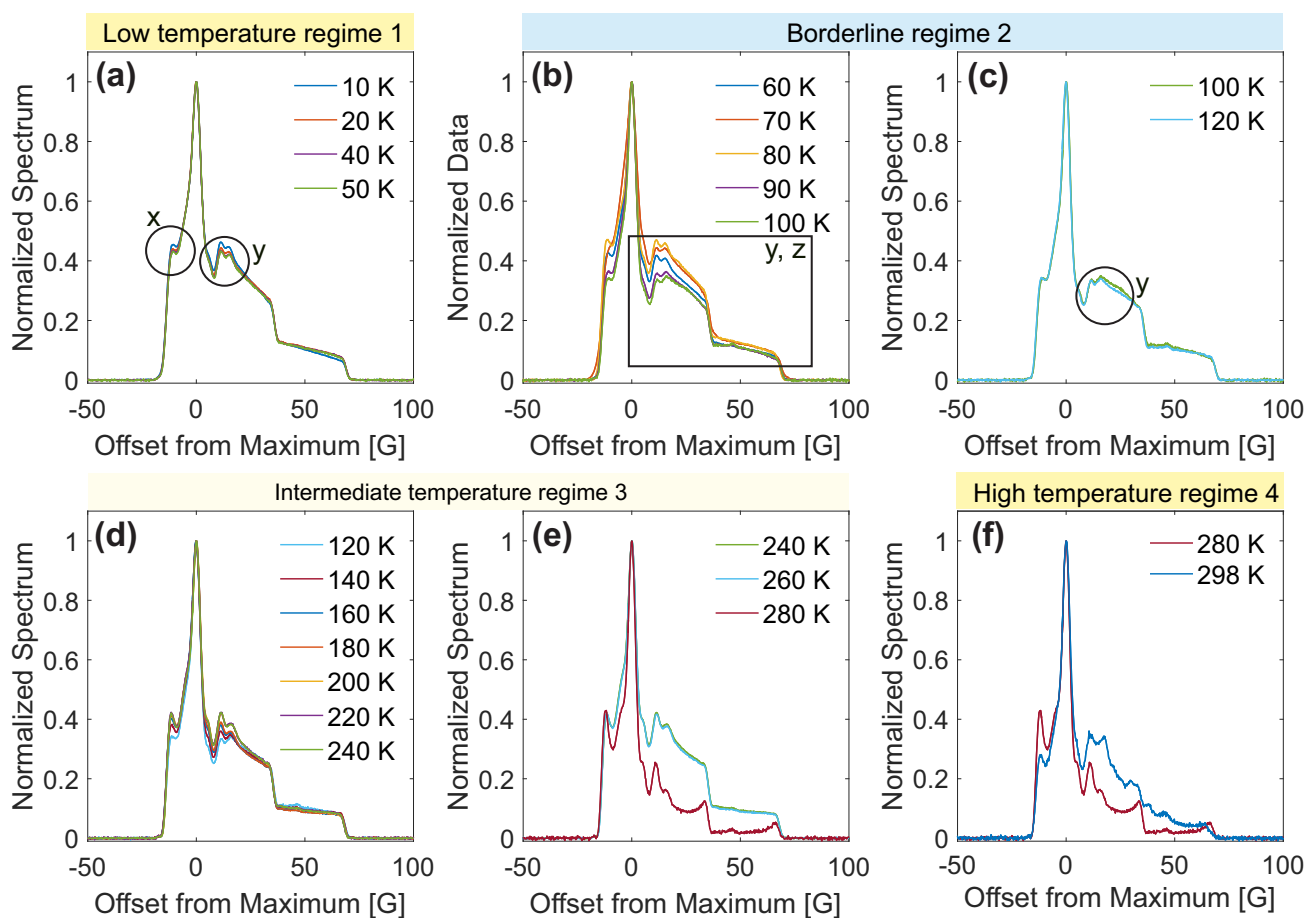


**Fig. S13.** Hahn echo detected field sweeps of 100  $\mu\text{M}$  nitroxide 2 in dOTP recorded with  $t_\pi = 2 \cdot t_{\pi/2} = 24$  ns as a function of temperature. The subfigures (a) to (f) serve for convenient comparison of spectral changes with respect to the marked temperature regimes (for definition of the latter see main text or Fig. S12). Each spectrum is normalized to its maximum, which serves as a reference point for the field offset axis. The features marked in (a) to (c) refer to the field positions at which the  $g$  principal values along the molecular frame  $x$ ,  $y$  and  $z$  axes can be found along with the hyperfine coupled  $^{14}\text{N}$  subensembles. For discussion on temperature dependent spectral features see sections 3.2.1 (low temperature regime 1, (a)) and 3.2.4 (high temperature regime 4, (f)) in the main text.

## 6 Relaxation traces to DD data sets at 40K

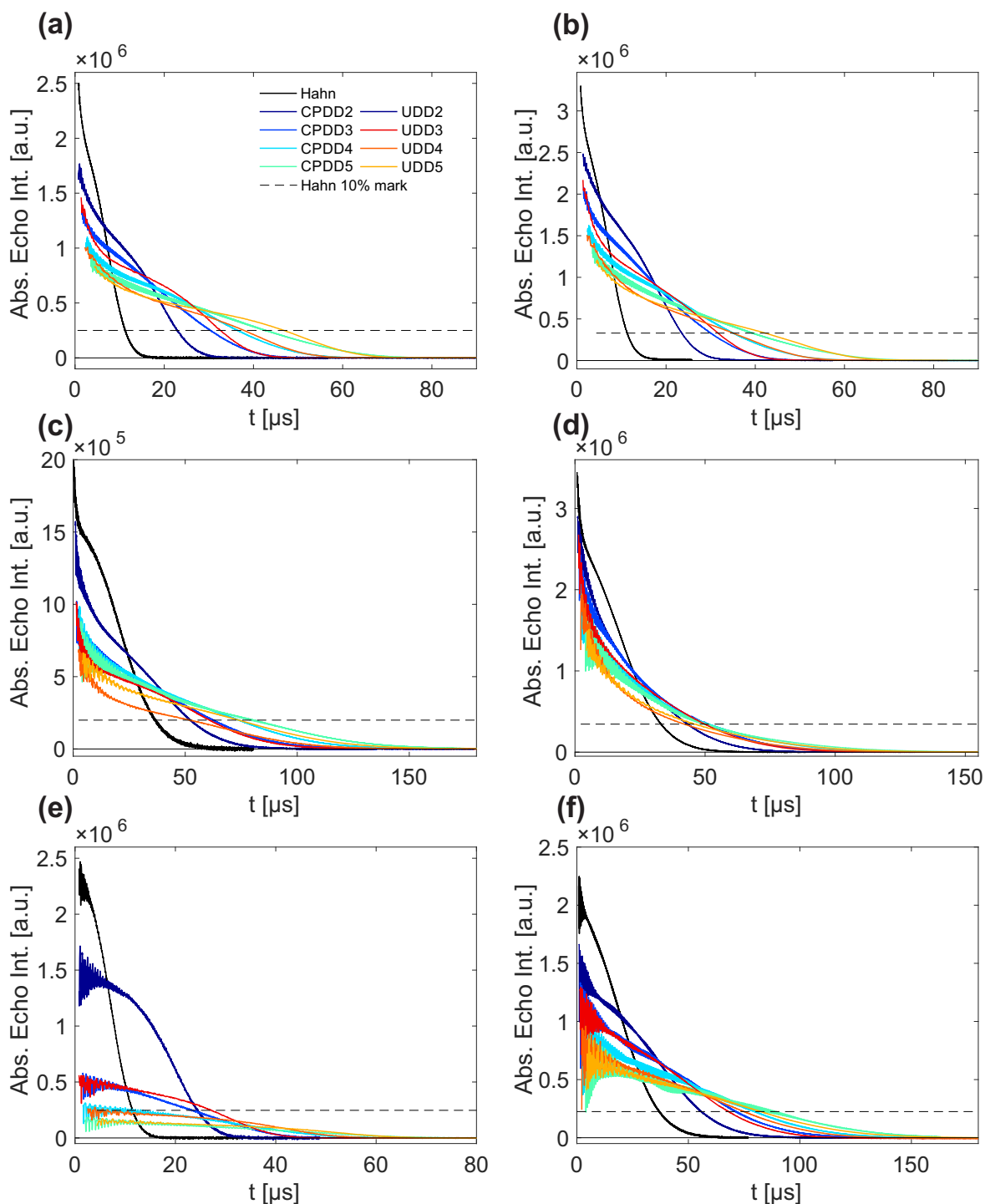


**Fig. S14.** DD data set at 40 K discussed under section 3.3.2 in the main text. Each row displays relaxation traces for a different sample with increasing level of deuteration going from top to bottom. Where (a) and (b) correspond to nitroxide 1 in OTP, (c) and (d) to nitroxide 1 in dOTP. The left and right column show 20 and 100  $\mu\text{M}$  sample concentration, respectively. In the last row both panels (e) and (f) correspond to 20  $\mu\text{M}$ , with nitroxide 2 in OTP being shown in (e) and nitroxide 2 in dOTP in (f). From the shown relaxation traces Fig. 8 in the main text was generated. The horizontal dashed lines mark 10% initial Hahn echo intensity for each data set, used to compute  $g_{\text{DD}}$  values, presented in Table 1 in the main text.

## 7 Relaxation traces to DD data sets at 80K

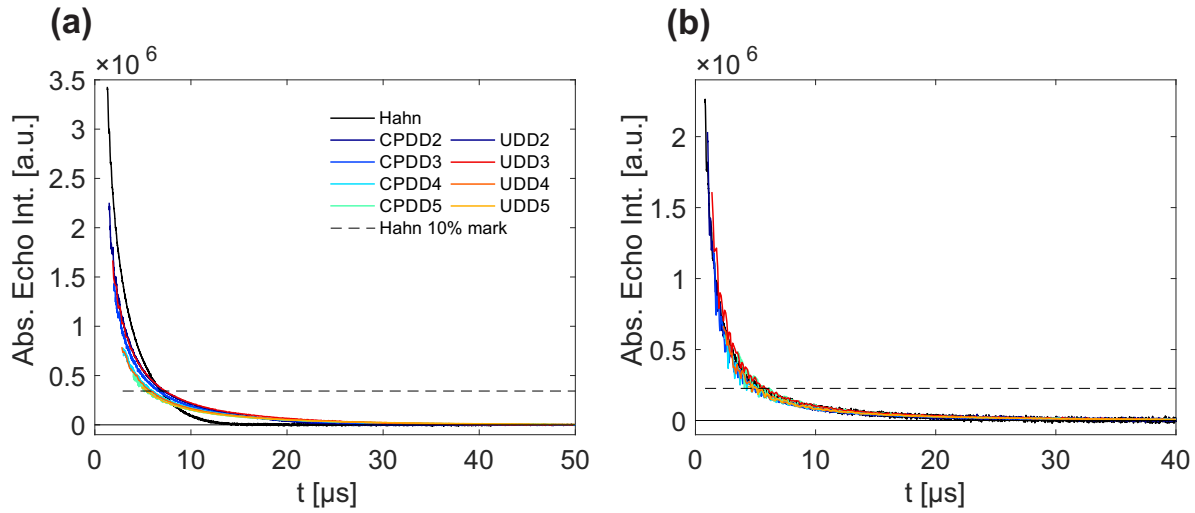


**Fig. S15.** DD data set at 80 K for 100  $\mu\text{M}$  nitroxide **1** in OTP **(a)** corresponding to a slight DD gain factor  $g_{\text{DD}}$  (defined in the main text) and **(b)** in dOTP illustrating a case for  $g_{\text{DD}} = 1$ .

## 8 Integral representation of normalized weighing factor $A_i$ in the SSE model

The stretched exponential function  $\exp[-(t/T_{m_i})^{\xi_i}]$  is a differential distribution describing the rate of relaxation as a function of time  $t$ . The first moment of this distribution is defined by

$$\langle T_m \rangle = \int_0^{\infty} \exp[-(t/T_m)^{\xi}] dt = \frac{T_m}{\xi} \Gamma\left(\frac{1}{\xi}\right). \quad (1)$$

For an exponential decay, *i.e.*  $\xi = 1$ , the first moment recovers the phase memory time  $\langle T_m \rangle = T_m$ .  $\langle T_m \rangle$  can be interpreted as the *mean phase memory time*. For the SSE model,  $V(t) = \sum_{i=1}^2 c_i \cdot \exp[-(t/T_{m_i})^{\xi_i}]$ , as introduced in the main text, the integral over the two relaxation contributions to the total echo day lead to two quantities  $I_i = c_i \langle T_{m_i} \rangle$  for  $i = 1, 2$ . Note, that the weighted mean phase memory times  $I_i$  does not carry new information but allows for a simplified representation of the SSE model. Whereas  $A_1$  serves as a normalized weighing factor,  $I_1$  corresponds to the spin fraction contributing via the fast relaxation pathway to the total echo intensity  $I_1 + I_2$  over time. As illustrated in Fig. S16, the trend for the  $n$  dependence of  $A_1$  can be qualitatively reproduced by the normalized  $I_1$  quantity. Fig. S16 shows only results derived from DD experiments in dOTP, as under these conditions the separability approach holds and the extraction of the SSE parameters  $c_i$  is reliable. Provided that  $\langle I_1 \rangle < 0.4 \cdot \langle I_2 \rangle$  applies, the normalized  $I_1$  quantity simplifies to a ratio of  $I_1$  and  $I_2$ . This is the case for nitroxide **2** in dOTP and the following considerations apply

$$\frac{I_1}{I_1 + I_2} \stackrel{I_1 \ll I_2}{\approx} = \frac{c_1 \langle T_{m_1} \rangle}{c_2 \langle T_{m_2} \rangle} = \frac{c_1 T_{m_1} \xi_2 \Gamma\left(\frac{1}{\xi_1}\right)}{c_2 T_{m_2} \xi_1 \Gamma\left(\frac{1}{\xi_2}\right)}$$

from Fig. 4(k) and (j) it follows

$$\frac{\xi_2 \Gamma\left(\frac{1}{\xi_1}\right)}{\xi_1 \Gamma\left(\frac{1}{\xi_2}\right)} \approx 1 \quad (2)$$

$$\frac{I_1}{I_2} = \frac{c_1 T_{m_1}}{c_2 T_{m_2}}.$$

Hence, according to equation (2) the ratio of the  $I_1$  and  $I_2$  is a linear function of the two phase memory times. As shown in Fig. S16 (d) and (e), the decoupling linearly increases the contribution

of the quickly decaying spins with increasing  $n$ , while  $I_2$  generally decreases. The same applies for nitroxide **1** in dOTP, while  $I_1$  and  $I_2$  are on the same order of magnitude

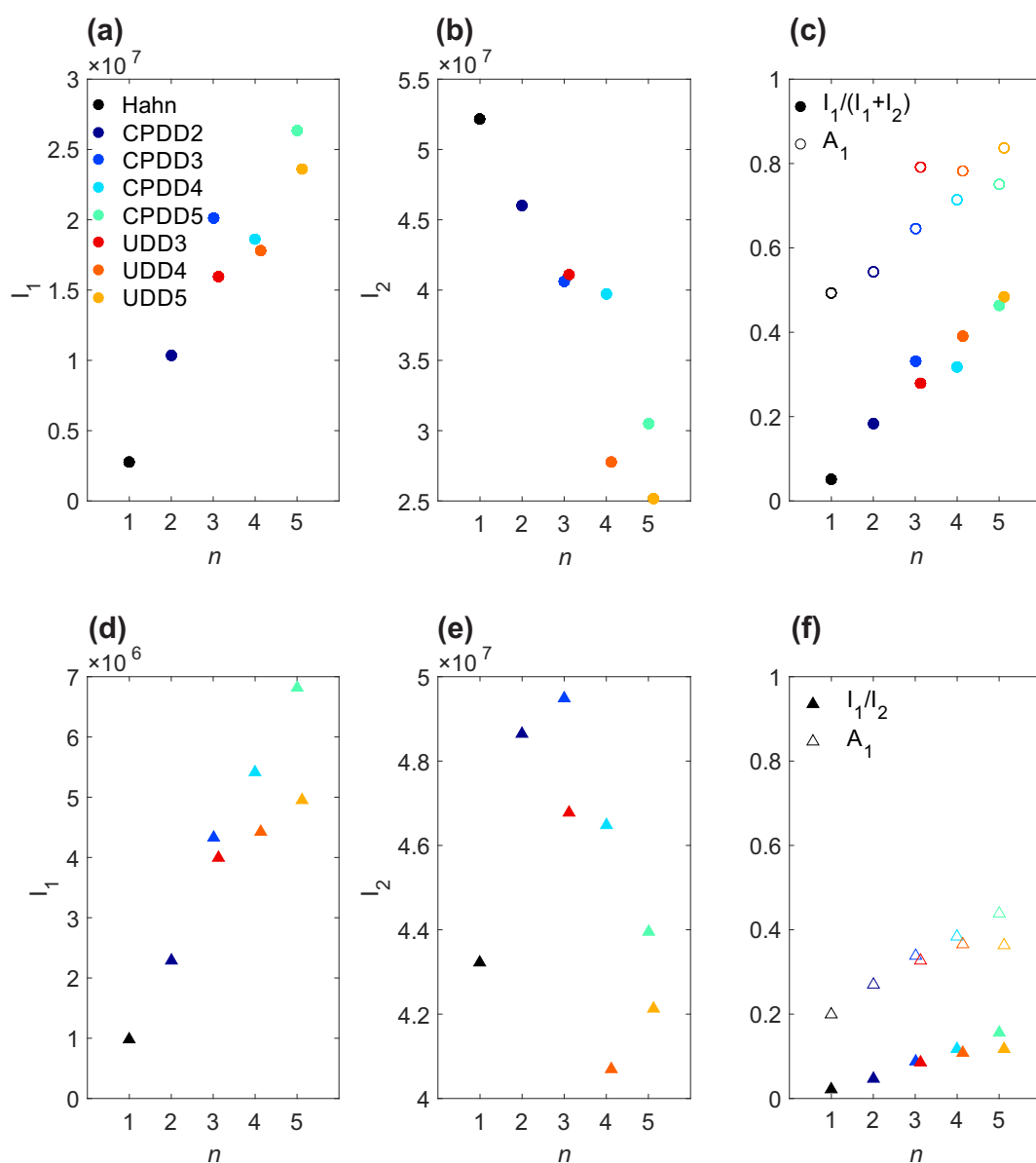


**Fig. S16.** Comparison between SSE model representation with normalized amplitude parameter  $A_1$  and weighted mean phase relaxation time  $I_i$  in **(c)** and **(f)** for  $100 \mu\text{M}$  nitroxide **1** and  $20 \mu\text{M}$  **2** in dOTP, respectively. **(a)** and **(b)** as well as **(d)** and **(e)** provide the quantities  $I_1$  and  $I_2$  as defined in equation 1. Note, that because of  $I_1 \ll I_2$  for nitroxide **2** in dOTP,  $\frac{I_1}{I_1+I_2} \approx \frac{I_1}{I_2}$  which does not apply for nitroxide **1** in dOTP.